Technische Universität München

Fakultät für Elektrotechnik und Informationstechnik

Lehrstuhl für Biologische Bildgebung

Studying nonlinear effects in optoacoustics

Jaber Malekzadehnajafabadi

Vollständiger Abdruck der von der Fakultät für Elektrotechnik und Informationstechnik der Technischen Universität München zur Erlangung des akademischen Grades eines Doktors der Ingenieurwissenschaften (Dr. –Ing) genehmigten Dissertation

Vorsitzender: Prof. Dr. Oliver Hayden

Prüfer der Dissertation:

1. Prof. Dr. Vasilis Ntziachristos
2. Prof. Dr. Werner Hemmert

Die Dissertation wurde am 01.10.2020 bei der Technischen Universität München eingereicht und durch die Fakultät für Elektrotechnik und Informationstechnik am 25.03.2021 angenommen.

Dedication
To my wife and my parents

Abstract

The reconstruction algorithm used in Optoacoustic imaging assumes that the detected signal varies linearly with light fluence and is exclusively proportional to the optical absorption coefficient of the medium. However, nonlinear variations in optoacoustic signal intensity have been observed within the first millimeter of tissue during optoacoustic microscopy studies. Optoacoustic signals behave nonlinearly above a specific light fluence threshold (approximately 6 mJ/cm^2), which may affect the interpretation and quantification of optoacoustic data. It has been suggested that the heat-induced formation of nanobubbles or changes in local thermo-physical parameters might explain this nonlinearity. However, such causes are unlikely to explain the observed nonlinearity at fluences of only a few mJ/cm2, typically used in biomedical optoacoustic imaging.

In this thesis, we investigate the nonlinear behavior of optoacoustic signals relating to optoacoustic mesoscopy and macroscopy, and characterize the fluence threshold required to delineate a switch from linear to nonlinear behavior. We observe fluence thresholds of approximately 6 mJ/cm^2 and preliminarily study the nonlinearity as a function of parameters such as optical absorption coefficient, reduced scattering coefficient, laser wavelength, and the molecular nature of absorbers in the imaged medium.

Moreover, we explore the temperature effects on optoacoustic nonlinearity. We show theoretically and experimentally that the light-induced local temperature rise does not cause nonlinearity in generated optoacoustic signals at room temperature, and that therefore the observed nonlinearity must be explained by other phenomena.

Next, starting from the electrostatic and thermodynamics concepts, we systematically investigate possible sources of optoacoustic pressure through theory and experiment, and introduce the concept of electro-optoacoustic pressure. We provide evidence that the major contributor to the observed nonlinear variations in optoacoustic signals at room temperature is the thermally excited nonlinear susceptibility that generates electro-optoacoustic pressure. We further develop a reconstruction algorithm to produce an image of thermally excited nonlinear susceptibility as a new contrast mechanism. These results may have far-reaching implications for our understanding of optoacoustics and for its application to basic and clinical sciences.

Lastly, we discuss the implications of nonlinearity in relation to image accuracy and quantification in optoacoustic tomography. We develop a correction algorithm to remove the nonlinear variations in optoacoustic signals, which enables the accurate reconstruction of optoacoustic images using only thermal pressure. At intermediate and higher fluences (> 6 mJ/cm^2), electro-optoacoustic pressure contributes more substantially to the measured optoacoustic signal. Therefore, the signal must first be corrected for electro-optoacoustic pressure in order to generate accurate reconstructions based on thermal pressure. These findings may help clarify nonlinear changes in optoacoustic signals and considerably improve the accuracy of optoacoustic tomography.

Abstrakt

Der bei der optoakustischen Bildgebung verwendete Rekonstruktionsalgorithmus geht davon aus, dass das erfasste Signal linear mit der Lichtfluenz variiert und ausschließlich proportional zum optischen Absorptionskoeffizienten des Mediums ist. Bei optoakustischen Mikroskopiestudien wurden jedoch nichtlineare Variationen der optoakustischen Signalintensität innerhalb des ersten Millimeters des Gewebes beobachtet. Optoakustische Signale verhalten sich nichtlinear oberhalb einer bestimmten Lichtfluenzschwelle (ca. 6 mJ/cm^2), was die Interpretation und Quantifizierung optoakustischer Daten beeinflussen kann. Es wurde vermutet, dass die wärmeinduzierte Bildung von Nanobläschen oder Änderungen lokaler thermophysikalischer Parameter diese Nichtlinearität erklären könnten. Es ist jedoch unwahrscheinlich, dass solche Ursachen die beobachtete Nichtlinearität bei Fluenzen von nur wenigen mJ/cm^2 erklären, die typischerweise in der biomedizinischen optoakustischen Bildgebung verwendet wird.

In dieser Arbeit untersuchen wir das nichtlineare Verhalten von optoakustischen Signalen im Zusammenhang mit optoakustischer Mesoskopie und Makroskopie und charakterisieren die Fluenzschwelle, die erforderlich ist, um einen Wechsel vom linearen zum nichtlinearen Verhalten abzugrenzen. Wir beobachten Fluenzschwellen von ungefähr 6 mJ/cm^2 und untersuchen vorab die Nichtlinearität als Funktion von Parametern wie dem optischen Absorptionskoeffizienten, dem reduzierten Streukoeffizienten, der Laserwellenlänge und der molekularen Natur von Absorbern im abgebildeten Medium.

Darüber hinaus untersuchen wir die Temperatureffekte auf die optoakustische Nichtlinearität. Wir zeigen theoretisch und experimentell, dass der lichtinduzierte lokale

Temperaturanstieg keine Nichtlinearität in erzeugten optoakustischen Signalen bei Raumtemperatur verursacht und dass daher die beobachtete Nichtlinearität durch andere Phänomene erklärt werden muss.

Ausgehend von den elektrostatischen und thermodynamischen Konzepten untersuchen wir systematisch mögliche Quellen des optoakustischen Drucks durch Theorie und Experiment und führen das Konzept des elektrooptoakustischen Drucks ein. Wir liefern Beweise dafür, dass der Hauptgrund für die beobachteten nichtlinearen Schwankungen der optoakustischen Signale bei Raumtemperatur die thermisch angeregte nichtlineare Suszeptibilität ist, die einen elektrooptoakustischen Druck erzeugt. Wir entwickeln einen Rekonstruktionsalgorithmus weiter, um ein Bild der thermisch angeregten nichtlinearen Suszeptibilität als neuen Kontrastmechanismus zu erzeugen. Diese Ergebnisse können weitreichende Auswirkungen auf unser Verständnis der Optoakustik und auf deren Anwendung auf die Grundlagen- und klinischen Wissenschaften haben.

Zuletzt diskutieren wir die Auswirkungen der Nichtlinearität auf die Bildgenauigkeit und Quantifizierung in der optoakustischen Tomographie. Wir entwickeln einen Korrekturalgorithmus, um die nichtlinearen Schwankungen der optoakustischen Signale zu entfernen, der die genaue Rekonstruktion optoakustischer Bilder nur unter Verwendung von thermischem Druck ermöglicht. Bei mittleren und höheren Fluenzen (> 6 mJ/cm^2) trägt der elektrooptoakustische Druck wesentlich mehr zum gemessenen optoakustischen Signal bei. Daher muss das Signal zuerst um den elektrooptoakustischen Druck korrigiert werden, um genaue Rekonstruktionen basierend auf dem thermischen Druck zu erzeugen. Diese Ergebnisse können dazu beitragen, nichtlineare Änderungen der optoakustischen Signale zu klären und die Genauigkeit der optoakustischen Tomographie erheblich zu verbessern.

Acknowledgement

First and foremost, I wish to thank my supervisor Professor Vasilis Ntziachristos for giving me the opportunity to work in this exciting field under his supervision. I would like to thank him for the stimulating discussions, for his trust, and for providing me the freedom to pursue my intuition. I appreciate his dedication to guiding and supporting me throughout my PhD.

I am greatly indebted to Dr. Jaya Prakash and Dr. Vipul Gujrati who were outstanding mentors, colleagues, and friends. They have helped me to view science from a different perspective, sharing their experience in research. I further appreciate Professor Jorge Ripoll for his helpful and encouraging comments.

I would also like to thank my colleagues at the institute for biological and medical imaging (IBMI), Helmholtz Zentrum München (HMGU), and TranslaTUM: Dr. Aguirre, Dr. Chmyrov, Dr. Gorpas, Dr. Juestel, Prof. Dr. Razansky, Dr. Stiel, Dr. Zakian, Dr. He, Dr. Huang, MD Karlas, Dr. Pleitez, Dr. Dean Ben, Dr. Mohajerani, Roman Shnaiderman, Mehdi Seyedebrahimi, Nian Liu, Antonia Longo, Qutaiba Mustafa, Ivan Olefir, Parastoo Afshari, Zak Ali, Yuanhui Huang, Kanuj Mishra, Markus Seeger, Antonios Stylogiannis who supported me and made this PhD a beautiful adventure. I would like to thank Pro. Dr. Bjoern H. Menze who supported me as a second supervisor.

I would like to thank the entire administrative group at IBMI for their help in all administrative matters during my PhD: Susanne Stern, Dr. Andreas Hillmair, Pro. Dr. Karl-Hans Englmeier, Dr. Roland Boha, Dr. Nike Tsalas, Dr. Christina Nagler, Dr. Julia Thomas, Ines Baumgartne, Dr. Bettina Lehman, Lidia Seidl, Dr. Doris Bengel, Dr. Manfred Tuerke. I appreciate Uwe Klemm, Sarah Glasl, and Pia Anzenhofer for their

exemplary assistance in the lab. I appreciate the editing assistance of Dr. Chapin Rodríguez, Dr. Robert Wilson, and Dr. Sergey Sulima.

I would like to thank all the BERTI partners who provided me with three years of medical training and a solid knowledge in biomedical imaging. The time I spent as an early stage researcher within BERTI gave me a tremendous amount of opportunities and support from many people. I would like to acknowledge Dr. Andrea Glogger, Dr. Katharina Lang, and Dr. Petra Dorfner who helped me with all administrative matters during the first three years, and all the BERTI ESRs: Mingming Wu, Yash Sharma, Teresa Rincon, Aurelien Bustin, Pedro Gomez, Suat Comert, Shufang Liu, Miguel Molina Romero, Saeed Seyyedi, Fatih Hafalir, Marwan Muhammad and Xin Liu who made this PhD a beautiful adventure. The exceptional interdisciplinary and international networks that BERTI offers, led me to travel and spend several months abroad. I am particularly grateful to Dr. Zacharakis Giannisand and Dr. George Tserevelakis for hosting me in Crete at the Institute of Electronic Structure and Laser (IESL).

I would also like to thank TUM, the European Commission under Grant Agreement no. 605162, the European Union's Horizon 2020 research and innovation programme under grant agreement no. 687866 (INNODERM), and the Deutsche Forschungsgemeinschaft (DFG) as part of the CRC 1123 (Z1) for their research support, without which this thesis would not have been possible.

Last but not least, I would like to express my deepest thanks to my parents, my brothers, and my sisters for always being supportive of my career and for their unconditional love. Research is a collaborative, but also very solitary, environment, which makes

such support invaluable. The constant support of my family and friends is what helped me complete my work. I also would like to thank my friend Mehdi Kazemi.

My most heartfelt appreciation is for my lovely and beautiful wife Mahsa Alizadeh, for all her love, wisdom, and support along this path. Mahsa has been extremely supportive of me throughout this entire process. I owe her everything.

Contents

1 Introduction

1.1 Biological imaging

Biological imaging is a fundamental tool for biomedical investigation to visualize the internal organs of the body and its diseases, for both in vivo and ex vivo studies, having wide ranges of applications spanning diagnosis to drug discovery and therapy monitoring. All biological imaging modalities can be characterized based on their penetration depth, temporal and spatial resolution, sensitivity and signal to noise ratio. A particularly useful characteristic for classifying biological imaging modalities is the type of the wave energy used to stimulate the tissue. Based on this criterion, biological imaging technologies can be classified in two main approaches. The first is non-optical modalities such as, positron emission tomography (PET), magnetic resonance imaging (MRI), ultrasound, and X-ray computed tomography (XCT) [1-4]. The second approach

is optical imaging such as fluorescence molecular tomography (FMT), bioluminescence tomography (BLT), and optoacoustic imaging [5-7].

Each of these imaging modalities has its own niche application, advantages and disadvantages (See Table 1.1). For example, some of the imaging modalities provide only anatomical/morphological information such as MRI and XCT, and while other modalities generated functional/molecular information such as PET and optical imaging methods [8]. However, the traditional imaging modalities like MRI, CT, and PET are not scalable in nature and there is a pressing need to develop a molecular imaging technique which is scalable i.e. can visualize sub-cellular structures to organ level information. In order to monitor structure and function simultaneously, two modalities can be integrated as a hybrid method such as PET-CT, FMT-XCT, optoacoustic-ultrasound (OPUS) or PET-MR [9-15]. In general, the goal of hybrid imaging techniques is to make up for a disadvantage of an imaging technique by adding complementary information.

Table 1.1 Advantages and disadvantages of various imaging modalities

Modality	Advantages	Disadvantages
MRI	• High depth penetration • Non-ionizing radiation • Whole body imaging	• Expensive • Time-consuming • Low resolution
PET	• High depth penetration • Whole body imaging	• Expensive • Time-consuming • Radiation Exposure • Low resolution
Ultrasound	• Real time imaging • Non-ionizing radiation • Low cost • Relatively good resolution	• Cannot be used for whole body
XCT	• High depth penetration • Whole body imaging	• Radiation Exposure • Low contrast for soft tissue • Low resolution
OI	• Real time imaging • Non-ionizing radiation • Low cost • High resolution	• limited depth penetration • Cannot be used for whole body

1.2 Optoacoustic imaging

Conventional optical imaging methods tend to get influenced by photon scattering (while imaging at depths greater than 1 mm) resulting in a reduced spatial resolution while recovering the optical contrast. Optoacoustic imaging is insensitive to photon scattering within biological tissue unlike conventional optical imaging methods thereby enabling us to obtain optical contrast at greater spatial resolution. Optoacoustic imaging is a recently invented hybrid imaging technique that takes advantages of both optical and acoustic imaging. Moreover, optoacoustic imaging makes high-resolution optical visualization from deeper regions possible by taking the advantage of the penetration of diffuse light and acoustic detection mechanism (as generated sound waves do not scatter) [16]. Lastly, optoacoustic imaging is a scalable imaging technique with potential of visualizing organelles to organ level information [17].

In optoacoustic imaging, optical energy is absorbed by absorbers such as hemoglobin, lipids, or other biological or functional absorbers in tissues [16]. Optical absorbers absorb photons proportional to their absorption coefficient and then they expand proportional to the local thermal expansion coefficient. These local expansions, known as initial pressure rise, gives rise to acoustic waves which propagate through the tissue and can be detected by one or an array of ultrasound transducers located at specific geometrical locations outside the sample [18]. The acoustic wave field propagation is modeled using the following wave equation, given as [18, 19]

$$\nabla^2 p(r,t) - \frac{1}{\mathrm{c}^2}\frac{\partial^2 \mathrm{p(r,t)}}{\partial \mathrm{t}^2} = -\Gamma \mu_{\mathrm{a}}(\mathrm{r})\frac{\partial I(r,t)}{\partial t} \tag{1.1}$$

where c is the speed of sound in tissue, Γ is the tissue-dependent Grüneisen parameter, μ_a is the optical absorption coefficient, I indicates the distribution of light intensity in the

imaging domain, r is the position in two-dimensional space, and t represents the time. The light intensity can be expressed as a product of its spatial and temporal components, i.e., $I(r,t) = I_r(r)I_t(t)$. In optoacoustic imaging, the laser pulse duration is on the order of 1-20 ns, and therefore $I_t(t)$ can be approximated by an impulse (delta) function. Consequently, an analytical solution for Equation (1.1) is given by a Poisson-type integral [18, 19],

$$p(r,t) = \frac{\Gamma}{4\pi c}\frac{\partial}{\partial t}\int_{l(t)=ct}\frac{H(r')}{|\mathrm{r}-\mathrm{r}'|}dl(t) \tag{1.2}$$

where $l(t)$ is the path, $H(r') = \mu_a(r')I(r')$, and $|\mathrm{r}-\mathrm{r}'| = \mathrm{ct}$ is the location of the spherical wave. In optoacoustic imaging, the pressure (p) is measured experimentally by rotating a single element transducer or using a transducer array and H (quantity of interest) is calculated by inverting Equation (1.2). Therefore, a reconstruction algorithm such as model-based algorithm is used to reconstruct the measured pressure to calculate the initial pressure distribution, which is proportional to the optical absorption map of the sample [20]. Consequently, the reconstructed images will have optical contrast at ultrasonic resolution. Diffusive media such as tissue strongly scatter and absorb incident photons, and this limits the application of traditional optical imaging technologies because it severely limits the depth to resolution ratio that can be achieved. Purely optical microscopy methods use ballistic photons which can penetrate few hundreds of microns, whereas optoacoustic imaging uses diffusive, unfocused light at near-infrared wavelengths, which can penetrate to several centimeters due to low light attenuation at near infrared wavelengths in biological tissue. Therefore, penetration depth of light will increase from few hundreds of micrometers, in pure optical microscopic techniques, to several centimeters, in optoacoustic imaging. The generated acoustic pressure wave is attenuated based on

the frequency, with higher frequencies attenuated more rapidly than low frequencies, in other words the recorded high frequency pressure wave can image shallower depths whereas low frequency pressure wave can image deeper regions.

This frequency-dependent attenuation can be used to generate images spanning different depths (volumes) of the sample, by selecting an appropriate transducer to detect acoustic signals of lower or higher frequencies [21, 22]. Optoacoustic macroscopy images over depths large enough to include nearly entire organs at relatively low resolution [23]; optoacoustic mesoscopy can image epidermis and the underlying dermal layers with sufficient resolution to distinguish individual hair follicles and blood vessels [24]; and optoacoustic microscopy can image extremely thin sections with very high resolution [25]. This potential for multi-scale imaging simplifies the development of hardware and software for diverse applications in basic biological research and biomedicine.

Another strength of optoacoustic imaging is that it can differentiate different molecules in the biological tissue based on the color of the molecules. When the sample is illuminated at multiple wavelengths, different chromophores, such as hemoglobin and lipids, can be identified by means of their unique absorption spectra. This is the approach taken in multispectral optoacoustic tomography (MSOT). In this case, the acoustic data is processed using spectral un-mixing algorithms to separate the contributions due to the different chromophores [26, 27]. The simplest un-mixing method is linear un-mixing [28], which may be challenging since the spectral profile of the agent may change in different biomedical environments, leading researchers to develop other un-mixing approaches [29].

With these characteristics, the optoacoustic modality can image in six dimensions: the three geometrical dimensions, time, optical wavelength, and ultrasound frequency [16].

1.3 Nonlinear optoacoustics

Nonlinear behavior in various imaging modalities have been reported to provide new applications or improve the image quality [30-37]. In optical imaging, nonlinear phenomena such as coherent anti-Stokes Raman scattering (CARS), second harmonic generation (SHG), and two photon excited fluorescence (TPEF) have attracted significant interest in various application in the recent years [30-32]. Besides, nonlinearity in ultrasound imaging was explored for tissue characterization purposes and improvement of agent-to-tissue ration [33-36]. Moreover, nonlinear effects in MRI as the nonlinear magnetic field was studied and nonlinear reconstruction was developed to produce high-quality images [37].

In this work, we focus on nonlinearities in optoacoustic imaging. According to the right-hand side of Equation (1.1) as the source term, the optoacoustic pressure is a function of three parameters: (1) the Grueneisen parameter, which reflects the thermo-physical properties of the medium and is a function of temperature; (2) the optical absorption coefficient, which reflects the optical properties of absorbers and can change at very high light intensities; and (3) the local light fluence, which is proportional to the number of photons that reache absorbers and can be controlled by adjusting the laser output. The optoacoustic signal changes linearly with variation of these three parameters as long as the local temperature remains constant and light fluence is sufficiently low [38]. However, it has been observed that the optoacoustic signal is nonlinear by increasing light fluence [39-43]. Different mechanisms have been used to explain this nonlinear behavior, such as the formation of nano-bubbles [39, 40] and changes of thermo-

physical parameters [43]. However, the main factors of the nonlinearity are not well explained. Therefore, a systematic study should be performed for understanding this nonlinear phenomenon and its main contributors. Also, the nonlinearity can have adverse effects on the reconstructed images, and no adequate algorithm exists to correct for such nonlinearity.

1.4 Goals and objectives

In general, the goal of this dissertation is to investigate alternative possible causes of nonlinear variation of the optoacoustic signal as a function of light fluence, used in biomedical optoacoustic imaging. The optoacoustic signal is supposed to change linearly with light fluence, but the optoacoustic signal measured from samples behaves nonlinearly after a specific light fluence threshold. We perform a systematic study to characterize and understand the nonlinear optoacoustics associated with diffusive light measurements. We investigate the factors of the setup and the medium that can have an effect on the nonlinearity in optoacoustics and what is the light fluence threshold to switch from linear to nonlinear behavior.

Moreover, we experimentally and theoretically interrogate the influence of the temperature on the optoacoustic signal to show if the light-induced local temperature rise can cause any nonlinearity in the recorded optoacoustic signal. In addition, we investigate the behavior of the recorded optoacoustic signal at temperatures close to zero degrees. Furthermore, we propose an alternative possible cause of the nonlinearities in optoacoustics by investigating the effects of the electric field on an absorptive dielectric media. Lastly, we examine the influence of the optoacoustic nonlinearity on the reconstructed images and develop an algorithm to remove the adverse effects of the nonlinearity from the measured data.

1.5 Outline of the Thesis

Chapter 2 will discuss the nonlinearity in optoacoustics as a function of light fluence. We will show the required threshold for light fluence to switch from linear to nonlinear optoacoustics. The chapter is planned based on a systematic study to show how some parameters affect the optoacoustic signal nonlinearity; these parameters include the optical absorption coefficient, the reduced scattering coefficient, laser wavelength, and the molecular nature of absorbers.

In chapter 3, we initially improve the experimental setup used in chapter 2 by removing complexity to have a better understanding of optoacoustic signal at macroscopic regime. Then, we investigate the nonlinearity at different time points from the newly acquired optoacoustic signal to test if the local temperature rise (variations in light fluence with depth) can explain the nonlinearity. We theoretically and experimentally examine the influence of temperature on the optoacoustic nonlinearity. At the end of this chapter, we report optoacoustic data acquired from a sample at a temperature close to zero degrees and frozen water (ice). In chapter 4, a new study is performed to investigate the main cause of the nonlinearity with a better understanding obtained from chapter 2 and 3. We initially explore the effects of the electric field on an absorptive dielectric media to hypothesize what might be the main contributor to nonlinearity. Then, we validate experimentally all our theoretical results and assumptions. Lastly, we conclude that the optoacoustic signal contains, in addition to thermal pressure, another component, which appears to be the primary cause of nonlinearity. We further studied if this second component can add any value for biological imaging.

In chapter 5, we use the better understanding of nonlinearity gained in chapter 3 to explore the effects of nonlinearity in MSOT. To interrogate the effects of nonlinearity in reconstructed images, we compare the reconstructed images of a phantom at low fluence and very high fluence. Then, we show the nonlinearity has some adverse effects on the reconstructed images. Consequently, we introduce a correction algorithm to remove the effect of the nonlinearity from the reconstructed data. In chapter 6, we conclude and review the results of this thesis and explain the next steps in optoacoustic nonlinearity.

2 Nonlinear optoacoustic readings from diffusive media at near infrared wavelengths

Content in this chapter is based on (at parts verbatim) the following journal paper:

- **Malekzadeh-Najafabadi J**, Prakash J, Ntziachristos V. “Nonlinear optoacoustic readings from diffusive media at near-infrared wavelengths.” J. Biophotonics, Volume 11, Issue 1, 2018.

2.1 Introduction

Optoacoustic imaging is among the widespread types of biomedical imaging with high optical resolution. The previous studies of optoacoustic imaging considered the detected optoacoustic signal to be linear with the light fluence delivered on the sample.

However, recent reports suggested optoacoustic signals behave nonlinearly in response to increasing light fluence on microscopic specimens [39-48]. Nonlinear signals have been measured from exogenous dyes, nanoparticles, and chromophores [39-42] and different mechanisms have been reported to explain the nonlinear behavior, including the formation of nano-bubbles [39, 40], changes of thermo-physical parameters, such as thermal expansion coefficient, due to local temperature enhancement around particles at high laser fluence [43], saturation of the absorption coefficient [42] or evaporation of fluids surrounding heated particles (250-355 °C for water) [39]. By using nonlinearity in optoacoustic microscopy, the absorbing target was differentiated over an absorbing background which generates a week linear response [40]. Nonlinear variations in optoacoustic signal was used to improve the lateral and axial resolution in optoacoustic microscopy [44, 48].

The dependence of the nonlinearity on wavelength and concentration has been reported in optoacoustic microscopy (using focused light beams) [49]. However, the nonlinearity has not been so far characterized in optoacoustic mesoscopy (broad-beam illumination). In addition, microscopy and mesoscopy operate at penetration depths of a few hundred micrometers and a few millimeters, respectively [50]. Therefore, mesoscopic and microscopic optoacoustic imaging are different in the operational characteristics. For this reason, the presence of nonlinear phenomena in mesoscopic optoacoustic imaging is explored in this chapter (diffusive light measurements).

This chapter organized as follows. The first measurement examines the presence of the nonlinearity within the mesoscopic samples. In the second measurement, we investigate the optoacoustic nonlinearity as a function of the optical absorption of the sample. The third measurement is performed to interrogate the influence of the

reduced scattering coefficient on the nonlinearity. The nonlinear responses of different optically absorbing substances, i.e. hemoglobin, ICG and India Ink and the nonlinearity dependence on wavelength are presented in the fourth and fifth measurements, respectively.

2.2 Method

2.2.1 Experimental Setup

To characterize the nonlinear effect in mesoscopic optoacoustic imaging, we used a simple experimental setup (Figure 2.1). In the experimental setup, the laser illuminates a cylindrical phantom located at the center of a circle region with 3.5 cm-diameter and 5 cm-height filled with water. To have uniform illumination on the sample, there was a separation of 3.5 cm between phantom and laser. To collect the optoacoustic data, we used a single element ultrasound transducer (Olympus, PZT) with a focal length of 3.5 cm, a central frequency of 3.5 MHz and a detector bandwidth of 90%. The signals were amplified (AU-1291 amplifier, L-3 Narda-MITEQ) and recorded using a data acquisition card (PCI-7340, NIC). For measurements, phantoms of 4.5 mm-diameter were inserted at the center of the field of view. Illumination comes from a tunable optical parameteric oscillator (OPO) laser (InnoLas Laser GmbH). A two sided illumination (with Gaussian beam profile) was achieved by guiding the light with a four-branch fiber bundle (WF 179, NA: 0.22, tip-Diameter: 2.5mm, CeramOptec GmbH) onto the phantom. To measure light energy, the other two fiber branches illuminated the optical sensor of a power meter (FieldmaxII-TOP, Coherent, CA, USA). Then, the measured energy is divided by illumination area at sample location to approximately calculate light fluence on the surface of phantom.

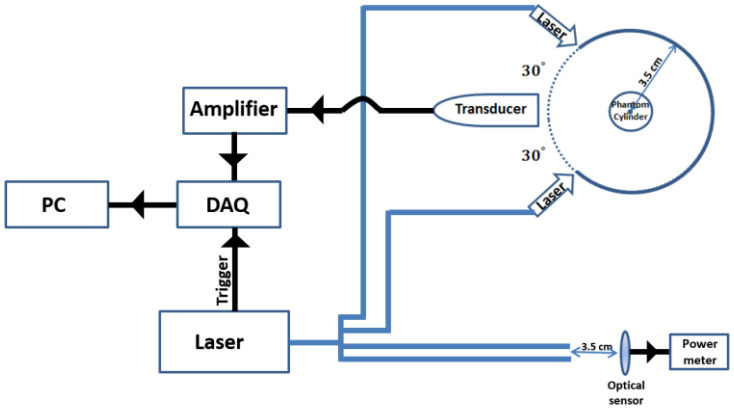

Figure 2.1: Schematic of the setup used for studying nonlinear optoacoustic effect.

2.2.2 Material

To prepare tissue mimicking phantoms, ink (Black India, Higgins, USA) was proportionally diluted in deionized water to have a phantom with a desired absorption coefficient, as determined by a spectrometer (LS-1-cal, USB4000, Oceanoptics, Germany). Different reduced scattering coefficient values were achieved by varying the concentration of the intralipid (20% emulsion, I141-100ML, SIGMA) in the mixture [51]. Lastly, two percent agar (05039-500G, Fluka, Spain) was added to the solution and heated in a microwave oven.

2.3 Experiments

2.3.1 Nonlinear characterization

The first measurement (MEAS-1) examined the generation of nonlinear optoacoustic signals in diffusive phantoms. The phantom was a 4.5 mm-diameter cylinder made of a mixture of ink, Intralipid and agar having an absorption coefficient of 0.23 cm^{-1} and a reduced scattering coefficient of 10 cm^{-1} at 800 nm. The optoacoustic signals were acquired at different light fluence. By using a high speed photodiode and an oscilloscope, the laser pulse was detected to examine the influence of laser pulse width on the nonlinearity at different laser energies.

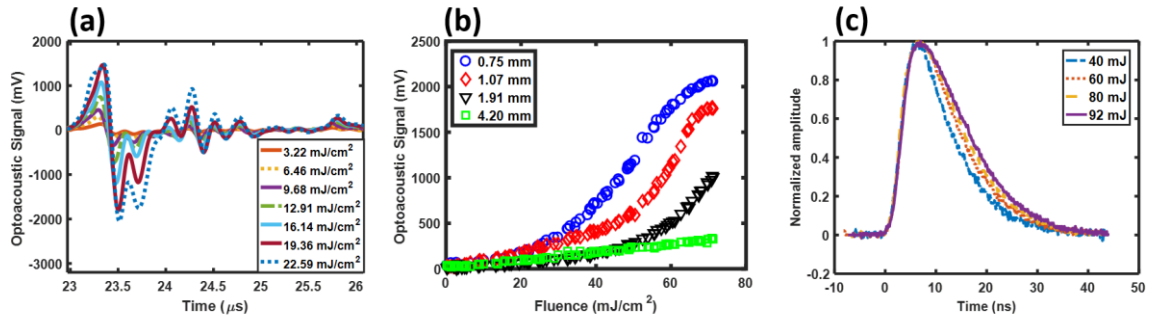

Figure 2.2: Raw optoacoustic signal from a mixture of ink, intralipid and agar phantom (MEAS-1) at different light fluence. (a) Raw optoacoustic data measured by the experimental setup. (b) Plot showing the absolute value of the optoacoustic signal at different depths 0.75, 1.07, 1.91, and 4.2 mm as a function of light fluence. (c) Laser pulse width measured with a photodiode at different laser energies.

Figure 2.2 depicts results that characterize the relationship between the light fluence and the optoacoustic signal detected at a wavelength 800 nm. Figure 2.2(a) plots the raw optoacoustic signals collected from an agar absorber (MEAS-1) in response to light fluence ranging from $3.22\ mJ/cm^2$ to 22.59 mJ/cm^2 increasing in steps of 3.23 mJ/cm^2. Figure 2.2(b) plots the absolute intensity of the signals as a function of light fluence at different depths of 0.75, 1.07, 1.91, and 4.2 mm, which correspond to time-points 23.5, 23.7, 24.3, and 25.8 μs in Figure 2.2(a), respectively. There is an initial linear response when the fluence is 0-8, 0-14, 0-16, and 0-23 mJ/cm^2 for depths of 0.75, 1.07, 1.91, and 4.2 mm, respectively. However higher fluence results in a nonlinear behavior for the depths of 0.75, 1.07, and 1.91 mm. Differences in the nonlinearity observed can be explained by the decreasing light fluence with depth in diffusive media. The response for the 4.2 mm depth is linear, which indicates that the light fluence reaching this depth is not sufficient for imparting nonlinear effects. Figure 2.2(c) illustrates the differences in laser pulse width observed are small (~ 4-5 ns). Therefore, the pulse width variation should not play a significant role in the results shown in Figure 2.2(b), because the stress relaxation time is typically much longer than

a few nanoseconds. Hence stress confinement is expected to be similar with the different pulse widths [52].

2.3.2 Effect of material concentration

In the second measurement (MEAS-2), the nonlinear behavior of the optoacoustic signal was investigated as a function of the absorption coefficient of the sample. We used three 4.5 mm-diameter agar cylinders which contained different amounts of India ink at concentrations that yielded absorption coefficient values of 0.46 cm^{-1} (0.2 OD), 0.23 cm^{-1} (0.1 OD), and 0.11 cm^{-1} (0.05 OD) at the wavelength 800 nm and the reduced scattering coefficient in all cases was 10 cm^{-1}.

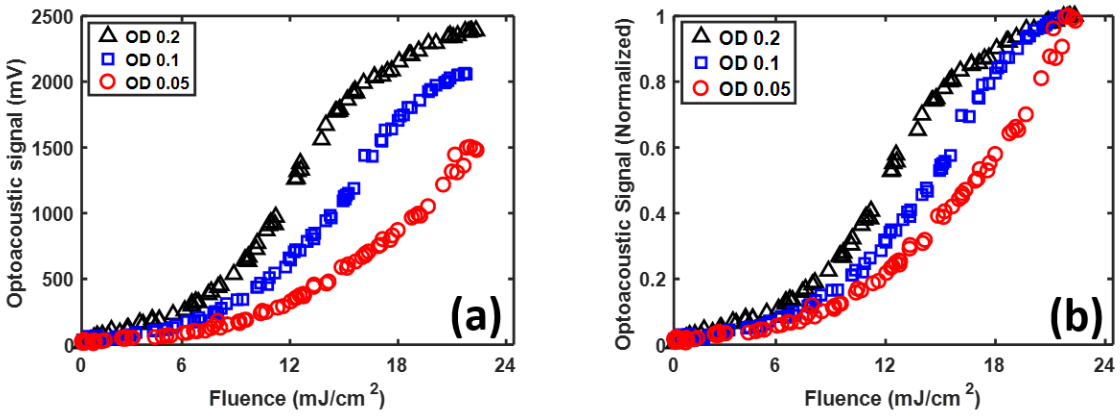

Figure 2.3 Optoacoustic signal variation over light fluence with different absorption coefficient: (a) Variation of measured optoacoustic signal from a mixture of ink, intralipid and agar (MEAS-2) at different light fluence and with different optical densities (OD) of Ink. (b) Normalized optoacoustic signal variation of Figure 2.3(a).

Figure 2.3 shows the results of MEAS-2, which studied the effects of absorber concentration on the optoacoustic signal as a function of light fluence at a wavelength of 800 nm. The detected optoacoustic signal exhibits a prominent nonlinearity with the increase of the absorption coefficient. Similar to the observation in Figure 2.2(b), all curves exhibit linear behavior for low fluence but a steeper ascend at higher fluence. At the upper part of light fluence employed we observe saturation effects. The

nonlinearity here follows a piecewise linear function and the slope of the second part of the piecewise linear function is bigger compared to first part of the function. In addition, as expected, a higher absorption coefficient generates a stronger optoacoustic signal. Figure **2.3**(a) depicts the raw signals, whereby Figure **2.3**(b) shows the same curves as in Figure **2.3**(a) but normalized to their maximum value.

2.3.3 Effect of Scattering

In a third measurement (MEAS-3), the nonlinear effect in optoacoustic signal was examined as a function of the optical reduced scattering coefficient in the phantom. The cylindrical phantoms with 4.5 mm-diameter were made of a mixture of agar and ink (imparting optical absorption with 0.05 OD at 800 nm) and intralipid (for optical scattering). The reduced scattering coefficients tested were: μ'_s =20 cm^{-1}, 15 cm^{-1}, 10 cm^{-1}. A control measurement was also obtained from a phantom that contained no scattering material.

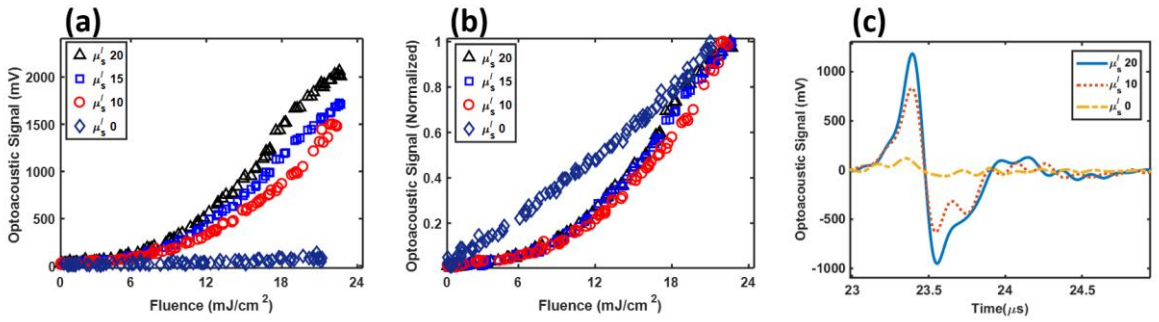

Figure 2.4 Optoacoustic signal variation over light fluence at different scattering coefficients: (a) Variation of the measured optoacoustic signal from a mixture of ink, intralipid and agar (MEAS-3) at different light fluence and with different reduced scattering coefficient (attained by varying Intralipid concentration). (b) Normalized optoacoustic signal variation of Figure 2.4(a). (c) Raw optoacoustic data for ink phantom with different reduced scattering coefficients acquired from measurement MEAS-3 when light fluence is $16\ mJ/cm^2$.

Results from MEAS-3, employed to characterize the relationship of the optoacoustic signal (amplitude) to the scattering coefficient are shown in Figure 2.4. The left panel (a) illustrates the nonlinear optoacoustic signal variation with increasing scattering coefficient and light fluence. A strong signal increase is observed for scattering media, compared to the non-scattering medium. Plotting the normalized profiles of the recorded signals exhibits that the optoacoustic signal in the non-scattering medium behaves linearly, however the optoacoustic signal trends for the scattering media are nonlinear and does not change by changing the scattering coefficient. The result indicates that scattering-related modifications in diffusive media change the responses expected as a function of fluence, compared to non-scattering media. Figure 2.4(c) plots the raw optoacoustic signals recorded for the different scattering schemes examined. The amplitude of optoacoustic signal for the non-scattering phantom is approximately an order of magnitude lower over the scattering medium, an observation that nevertheless depends on the divergence and spatial distribution characteristics of the illuminating beam employed. All measurements were done at 800 nm.

2.3.4 Nonlinearity of different materials

We acquired the optoacoustic signal from different materials (ink, indocyanine green (ICG) and hemoglobin) to test the nonlinear effect as a function of different optically absorbing material (MEAS-4). We prepared three different 4.5 mm-diameter cylinders containing blood, ICG or India ink mixed with agar. The amount of absorbing material employed was adjusted so that the absorption coefficient in the cylinders was $\mu_a = 0.23$ cm^{-1} at 800 nm, for all three materials studied. No scattering material was employed in the phantom, so that the effect of material is studied independently of scattering effects.

Figure 2.5(a) depicts the signals collected from the three materials as a function of light fluence at a wavelength of 800 nm. It is clearly observed that the materials exhibit different

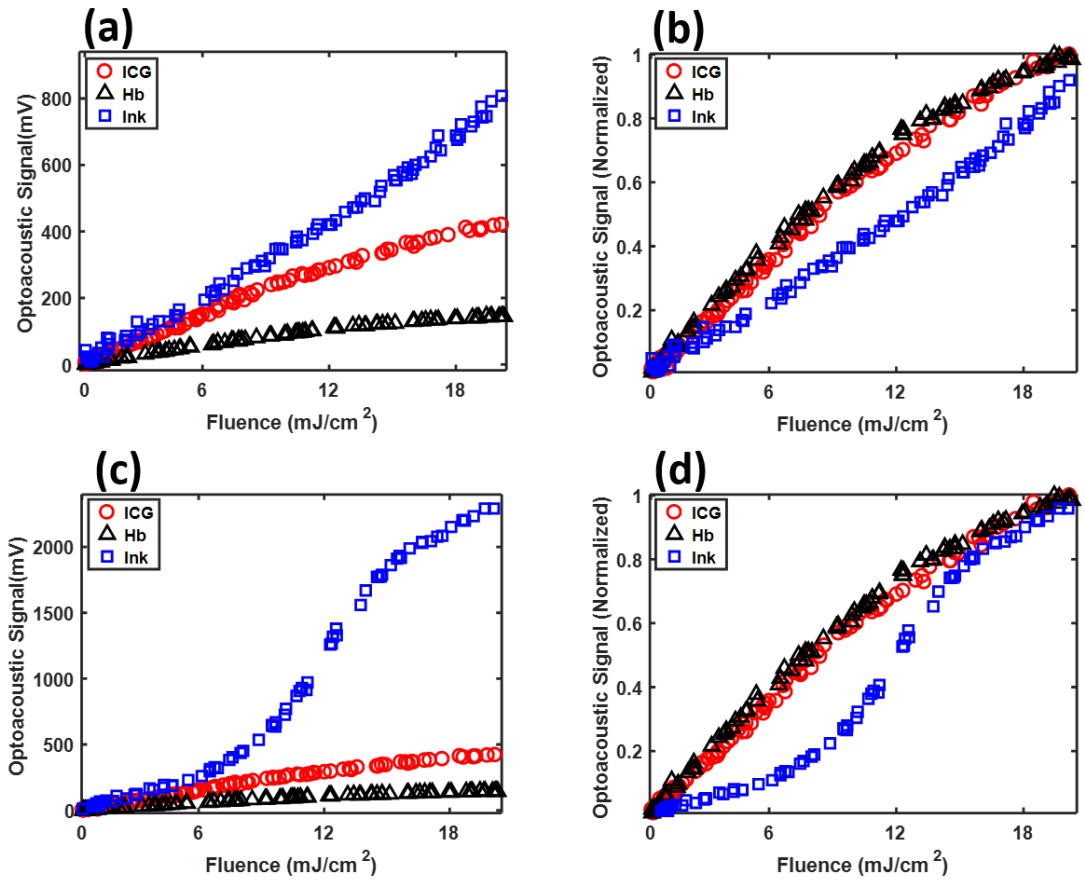

Figure 2.5 Optoacoustic signal variation over light fluence with different materials: (a) Variation of measured optoacoustic signal at different light fluence and with different materials (Hemoglobin, India Ink, Indocyanine Green (ICG)). There was no scattering in the media measured. (b) Normalized optoacoustic signal variation of Figure 2.5(a). (c) Variation of measured optoacoustic signal at different light fluence and with different materials with same absorption coefficient $\mu_a(r) = 0.23\ cm^{-1}$ at 800 nm and different reduced scattering coefficient, Hemoglobin (diluted mouse blood), India Ink ($\mu'_s(r) = 10$), Indocyanine Green ($\mu'_s(r) = 0$)). (d) Normalized optoacoustic signal variation of Figure 2.5(c).

nonlinear responses. Ink follows a linear behavior, as demonstrated in Figure 2.4. However, hemoglobin shows a steeper initial increase, which then exhibits early

saturation effects, evident on the normalized plot shown in Figure 2.5(b). ICG follows a response similar to hemoglobin. Figure 2.5(c) illustrates the result acquired from the blood phantom, ICG phantom and ink phantom (only ink phantom had scattering, reduced scattering coefficient of 10 cm^{-1}). The response from the ink phantom confirms the observations in Figure 2.4. Figure 2.5(d) depicts the normalized plot of Figure 2.5(c) for better comparison of nonlinearity in the three materials examined.

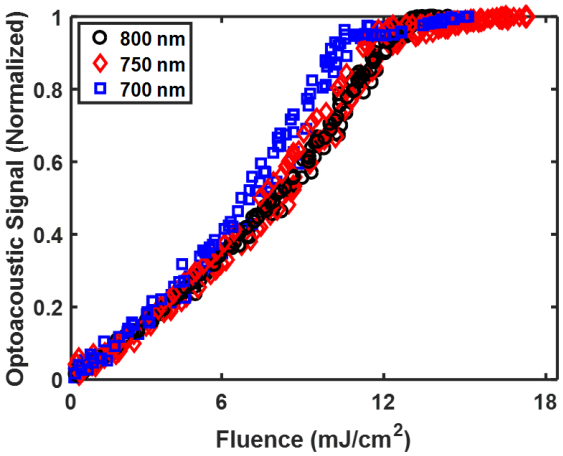

Figure 2.6 Strength of optoacoustic signal from ink phantoms at different light fluence and wavelengths (MEAS-5). The graph shows the results obtained at three different wavelengths, normalized to their respective maximum values.

2.3.5 Measurements at different wavelengths

We explored the optoacoustic nonlinearity as a function of light wavelengths. We prepared three 4.5 mm-diameter agar cylinders with different India ink concentrations adjusted to yield the same absorption coefficient of 0.46 cm^{-1} at all wavelengths examined, i.e. 700 nm, 750 nm, and 800 nm. The three cylinders were then measured (MEAS-5) at the corresponding wavelengths they were prepared for. Each measurement was repeated 3 times. The phantoms in this case have no scattering to remove effect of scattering at different wavelengths. For each wavelength results from three consecutive measurements (1h apart) were normalized to maximum signal

values (Figure 2.6). The results show different optoacoustic signal intensity trends as a function of wavelength. Optoacoustic signal attained saturation at 11 mJ/cm^2 at 700 nm, 12 mJ/cm^2 at 750 nm, and 13 mJ/cm^2 at 800 nm. These findings may relate to energy differences of photons between wavelengths, since photons at lower wavelengths have higher energy.

2.4 Discussion and conclusion

In this chapter, optoacoustic nonlinearity was explored in optoacoustic mesoscopy as a function of OD changes (absorption), scattering changes and in relation to the material and wavelength employed. We have shown that nonlinear effects can be observed at light fluences that are typically employed for imaging purposes.

It is interesting to note that the optoacoustic signal significantly increase by adding scattering to the phantoms. Moreover, nonlinear effects were not evident in non-scattering material (Figure 2.4). A possible explanation for this observation relates to the light propagation pattern inside the phantom. Since the distribution of light inside the non-scattering phantom follows propagation along diverging straight lines, the effective absorption cross-section and excitation energy deposited on the absorber is less than in diffusive light propagation, which allows multiple interactions between photons and the absorber.

Different nonlinearity trends were observed in different materials, implicating involvement of the molecular nature of absorbers. In addition, nonlinearity was a function of light wavelengths (i.e. Figure 2.6 at 700 nm, 750 nm and 800 nm) and may be associated with the different energy of photons at different wavelengths.

Since the standard reconstruction algorithms assume the optoacoustic signal is a linear function of fluence, our observations suggest that the conventional reconstruction algorithms for optoacoustic imaging may be less accurate at light fluence above ~ $6\ mJ/cm^2$ as a certain threshold which relies on measurement under the Maximum Permissible Exposure (MPE) limits [53]. The nonlinearity observed was found in superficial layers at depths < 2 mm for our phantoms (Figure 2.2(b)), but the significance of the observed nonlinearity extend to the entire image during reconstruction from collected optoacoustic data at mescoscopic scales. Since we reconstruct the entire field of view (both at the mesoscopic and macroscopic regimes), the dynamic range of the entire imaging domain will be affected due to observed nonlinearity [20, 54-56]. In chapter 5, we develop a correction algorithm for the nonlinear response to improve tomographic quantification when using pulses of higher energy. Since the generation of optoacoustic signals depends on more parameters of the medium, including the optical and thermo-physical parameters, then in chapter 3 and 4, we examine additional factors that may contribute to nonlinear optoacoustics.

3 Temperature effects on optoacoustic data

3.1 Introduction

In this chapter, we investigate the influence of temperature on the optoacoustic signal and examine the nonlinearity as a function of the laser-induced local temperature rise. The optoacoustic nonlinearity has been explained by temperature dependence of the thermal expansion coefficient [39, 46, 57, 58]. We show that the local temperature rise might not be the main factor of the optoacoustic nonlinearity when the probed medium has room temperature.

To better understand optoacoustic nonlinearity, we improved the experiments and experimental setups used in the second chapter by removing complexity. We altered three features of the previous phantoms and experimental setup (Figure 2.1). First, we

increase the size of the phantoms to have tomographic samples instead of mesoscopic samples. Second, a transmission mode setup was used (Figure 3.1a). Third, cubic phantoms were used to have a simple geometry. By doing these three modifications, we acquired a simple bipolar optoacoustic signal which makes it easier to analyze and investigate optoacoustic nonlinearity. We have initially investigated nonlinear optoacoustic effects at different time points of the acquired optoacoustic signal and observed different nonlinear behavior which could not be explained by variations in the light fluence as a function of depth. Moreover, we found that the light-induced variations in the optoacoustic signal caused a time shift in the measured optoacoustic signal. We show the observed time shift leads to the interpretation that the width of the phantom shrinks with increasing fluence according to the measured optoacoustic signal. Ideally if the temperature changes induce nonlinearity we would expect the “expansion” to be aggravated, however we observed an opposite behavior of compression of the sample. Therefore, we explored the influence of temperature on nonlinear optoacoustics and the generated optoacoustic signal by controlling the temperature of the media. We showed theoretically and experimentally that the light-induced local temperature rise cannot cause any nonlinearity in the generated optoacoustic signal at room temperature and the observed nonlinearity should be explained by other phenomena. Moreover, we observed the optoacoustic signal behaves nonlinear at temperatures close to zero degree Celsius while it is linear at higher temperatures (> 10 degree Celsius). In the last section, we show the discrepancy between the optoacoustic spectra and reconstructed image of deionized water and ice (frozen water), using a multispectral optoacoustic tomography scanner (MSOT256-TF; iThera Medical, Germany; Figure 3.1b).

3.2 Method

3.2.1 Experimental Setup

To investigate the influence of temperature on the nonlinear optoacoustic phenomenon in a phantom, the result of which is shown in Figure 3.3-Figure 3.5, we used the experimental setup shown in Figure 3.1a. The cubic phantom was aligned with the transducer and with the illumination source inside a chamber filled with deionized water. The cubic phantom was illuminated using a tunable optical parametric oscillator (OPO) laser (InnoLas Laser, Germany). The cubic phantom and the optical sensor of a power meter (PE50BF-DIF-C RoHS, OPHIR, Darmstadt, Germany) were located at the same distance (2.4 cm) from the illumination source to be able to measure accurately the fluence on the surface of the phantom. To achieve the same illumination (with a Gaussian beam profile) on the surface of the optical sensor and phantom, a four-branch fiber bundle (WF 179, numerical aperture 0.22, tip diameter 2.5 mm; CeramOptec GmbH, Bonn, Germany) was used in which two branches were blocked and the other two guided the light to the phantom and the sensor separately. To calculate the light fluence on the surface of the phantom, the measured energy was divided by the illumination area on the surface of the phantom. A separation of 2.8 cm between the phantom and the transducer was used to locate the phantom at the focal area of the transducer. The optoacoustic signal was collected using a single-element transducer (Olympus, PZT, Waltham, MA, USA), with a focal length of 3.5 cm, central frequency of 3.5 MHz, and detector bandwidth of 90%. The signals were amplified using an AU-1291 amplifier (L-3 Narda-MITEQ, Hauppauge, NY, USA) and recorded using a data acquisition card (PCI-7340, National Instruments Corporate, USA). Each phantom was built three times and each measurement was performed three times for each phantom.

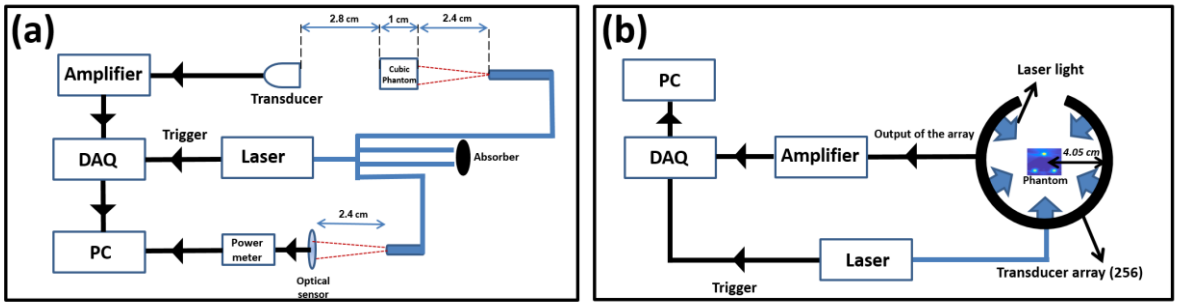

Figure 3.1. Schematic of the set-ups used to study the influence of temperature on optoacoustic data. (a) The set-up used to collect optoacoustic signal from homogeneous diffusive phantoms, for which the experimental results are shown in Figure 3.3-Figure 3.5. (b) The set-up used to collect optoacoustic signal from the liquid deionized water and frozen water (ice), for which the results are shown in Figure 3.6.

To examine the optoacoustic spectra and reconstructed image of liquid water and frozen water (ice), the results of which are shown in Figure 3.6, a small-animal multispectral optoacoustic tomography scanner (MSOT256-TF; iThera Medical, Germany) and imaging setup shown in Figure 3.1b were used. This imaging system has been described in detail elsewhere [59]. A tunable OPO laser (InnoLas Laser) homogeneously illuminated a water-filled field of view with a diameter of 4.05 cm from five directions. The phantom was homogeneously illuminated from all directions. These signals were detected using a 256-element ultrasound transducer array with a central frequency of 5 MHz and a detector bandwidth of 90%. Signals were amplified and recorded using a data acquisition card [59].

To verify the linear response of the experimental setup (Figure 3.1a), we used a 3.5 MHz-flat transducer (Transducer-1, Olympus, PZT, Waltham, MA, USA) which operates as an acoustic source (Figure 3.2). The input of Transducer-1 is a pulse signal that is generated by a signal generator.

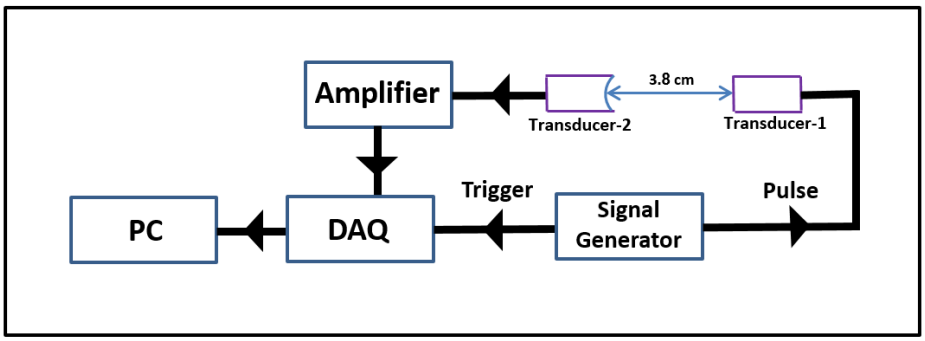

Figure 3.2. Testing the impact of the setup on the measurements. (a) The experimental setup used to investigate the behavior of the components.

3.2.2 Material

The homogeneous agarose phantoms were prepared as cubes ($1 \times 1 \times 1$ cm) by mixing agar (2% solution in deionized water, 05039-500G, Sigma-Aldrich, Steinheim, Germany) with black India ink (Higgins, Texas) and intralipid (20% emulsion, I141-100ML, Sigma). The mixture was prepared as described in Section 2.2.2.

3.3 Fluence and nonlinearity

Firstly, we examined and characterized the existence of nonlinearity at different time points of the optoacoustic signal as a function of light fluence. We assessed the behavior of the detected optoacoustic signal from an optically diffusive phantom at different depths as a function of fluence. A homogeneous agar cube with uniform absorption coefficient $\mu_a = 0.1\ \mathrm{cm}^{-1}$ and reduced scattering coefficient $\mu_s' = 4\ \mathrm{cm}^{-1}$ was illuminated with various fluences at 800 nm in transmission mode (Figure 3.1(a)). The resulting optoacoustic signals featured a first rising front corresponding to the pressure generated in the part of the cube closer to the transducer (edge A), followed by a second front corresponding to the pressure generated in the part closer to the illumination source (edge B; Figure 3.3(a) and Figure 3.3(b)). The signal at the first

front was relatively weak due to light attenuation through the phantom, whereby the signal at the second front was stronger, as it was illuminated with a non-attenuated fluence.

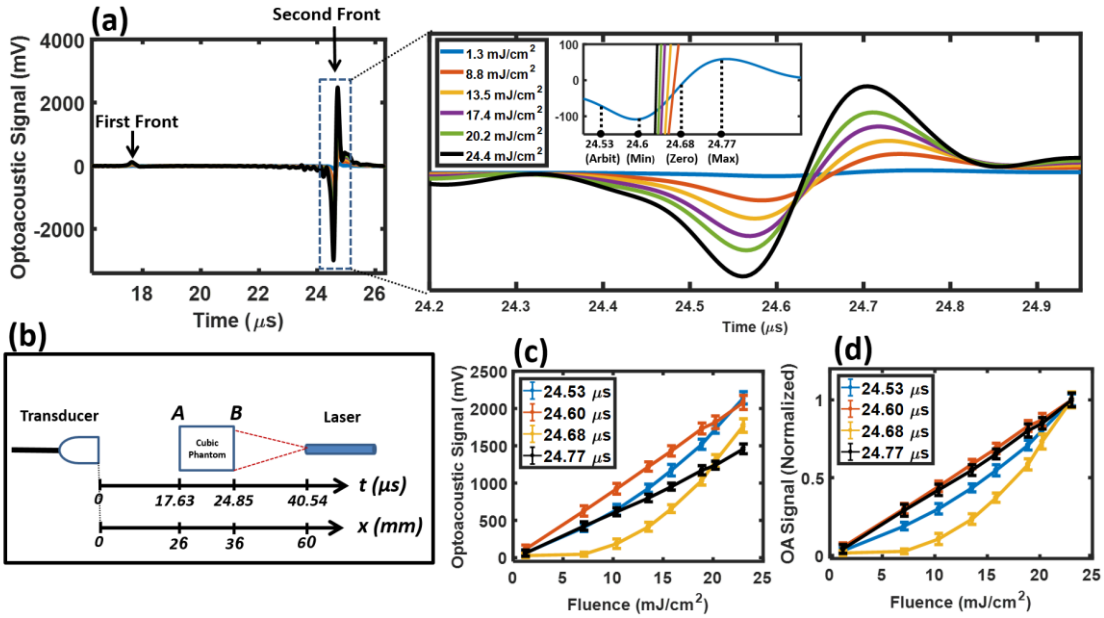

Figure 3.3.Exploring nonlinear optoacoustic response at various time points as a function of fluence. A homogeneous agar cube with uniform absorption coefficient $\mu_a = 0.1\ \mathrm{cm}^{-1}$ and reduced scattering coefficient $\mu_s' = 4\ \mathrm{cm}^{-1}$ was illuminated with various fluences at 800 nm. (a) Raw optoacoustic data. Signals corresponding to the first edge (closer to transducer) or second edge (closer to illumination source) are labeled. The inset plot shows the signal from the second edge in greater detail. (b) Phantom location in the setup based on time and distance axis. (c) Absolute value of the optoacoustic signal at different time points as a function of light fluence. (d) The same data as in panel (c) after normalization.

Possible nonlinearity in the signal was examined at four time points of the recorded signal corresponding to the minimum, maximum, zero-crossing and an arbitrary point of the signal at the second front (edge B; Figure 3.3a, inset). We found that the optoacoustic signal increased linearly as a function of fluence at 24.60 and 24.77 μs,

but nonlinearly at 24.53 and 24.68 μs (Figure 3.3c-d). The signal showed stronger nonlinearity at 24.68 μs than at other time points. In other words, nonlinearity was negligible at the inflection (peak) points (24.60 and 24.77 μs) of the second front of the signal (edge B), maximal at the x-intersect (24.68 μs) of the second front of the wave, and intermediate at another point (24.53 μs). These results suggest that nonlinearity is not explained by variations in fluence with depth because fluence at the depth corresponding to time point 24.53 μs is less than time point 24.60 μs, yet the signal showed nonlinearity at 24.53.

3.4 Light-induced time shift

Moreover, we performed an experiment to examine temperature effects on nonlinearity in the measured optoacoustic signal. We examined whether the distance between the first and second front of the optoacoustic signal observed with an agar cube phantom (Figure 3.3(a) and Figure 3.3(b)), corresponding to the width of the phantom, would change with increasing fluence. An increase of the apparent width with fluence could suggest heating-induced expansion of the medium, i.e. a temperature rise that may contribute to observed nonlinear optoacoustic behavior. Figure 3.4(a) shows the normalization of three optoacoustic signals from Figure 3.3(a) at fluence values of 1.3, 13.5, and 23 mJ/cm2. Figure 3.4(b) and Figure 3.4(c) show the first and second fronts in greater detail. The peak at the first front occurs at the same distance of 25.76 mm for all three fluence values, whereas there is a leftward time shift for the peaks at the second front, which occurs at a distance of 36.13 mm for a fluence of 1.3 mJ/cm^2, 36.08 mm for a fluence of 13.5 mJ/cm^2 and 36.03 mm for a fluence of 23 mJ/cm^2. In other words, the peak at the second front shifts more towards the first front as fluence increases: the distance between the two edges is 10.37 mm at 1.3 mJ/cm2, 10.32 at

13.5 mJ/cm2, and 10.27 mm at 23 mJ/cm2. This indicates that the width of the phantom "shrinks" with increasing fluence. This is the opposite to the notion of phantom expanding more due to the nonlinear behavior observed when the temperature changes.

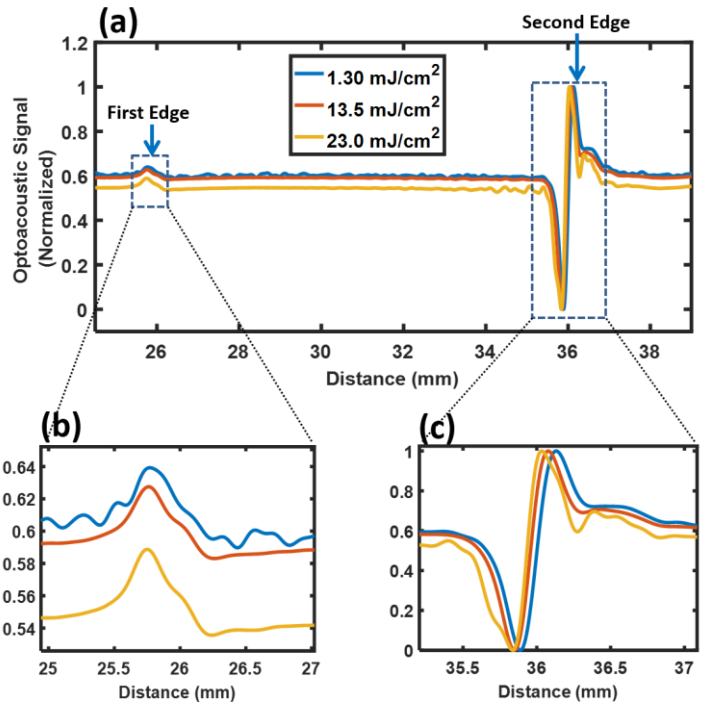

Figure 3.4. The normalization of the optoacoustic signal at different light fluence. A homogeneous agar cube with uniform absorption coefficient $\mu_a = 0.1\ \mathrm{cm}^{-1}$ and reduced scattering coefficient $\mu_s' = 4\ \mathrm{cm}^{-1}$ was illuminated with various fluences at 800 nm. (a) Normalized raw optoacoustic signal at three light fluence values 1.3, 13.5, and 23 mJ/cm^2. (b) The optoacoustic signal generated at the edge of the cube closer to the transducer named first edge. (c) The optoacoustic signal corresponding to the second edge of the cube closer to the illumination source named second edge.

3.5 Temperature and nonlinearity

In optoacoustics, the generated acoustic pressure is a function of thermo-physical parameters of the sample such as, thermal expansion coefficient (β), speed of sound (v), and specific heat capacity (C_p). These three thermo-physical parameters often

appear in the combination $\frac{\beta v^2}{C_p}$ which is called Grueneisen parameter. Therefore, the optoacoustic signal is strongly a function of temperature due to temperature dependence of thermo-physical parameters. In this section, initially, we investigate theoretically the influence of the temperature on optoacoustic pressure. These theoretical considerations led us to hypothesize that temperature rise is unlikely to explain the optoacoustic nonlinearity. We explored this hypothesis in an experiment using phantoms and imaging conditions typical of those used in basic and clinical optoacoustic imaging.

3.5.1 Theory

To investigate the effects of temperature on optoacoustic nonlinearity, we have to calculate optoacoustic pressure as a function of temperature. If we neglect the term $\nabla^2 p$ in Equation (1.1) for time periods shorter than the stress relaxation time, i.e. periods whereby only a negligible fraction of the pressure travels out of the interaction region, we can rewrite Equation (1.1),

$$\frac{\partial^2 p}{\partial t^2} = \Gamma \mu_a \frac{\partial I}{\partial t} \tag{3.1}$$

By defining light fluence by using $\varphi = \int \mathrm{I(t)dt}$, we have

$$p = \Gamma \mu_a \varphi \tag{3.2}$$

By considering Grueneisen parameter as a nonlinear function of temperature, we can write

$$\Gamma \approx \Gamma|_{T=T_0} + \left.\frac{\partial \Gamma}{\partial T}\right|_{T=T_0} \Delta T \tag{3.3}$$

where T0 is equilibrium temperature of the sample and ΔT is the variation of temperature due to absorption of light that can be calculated using the conservation of energy equation,

$$\frac{\partial}{\partial t}\left[k_0\nabla^2 T - \rho C_p \frac{\partial T}{\partial t}\right] - \beta T_0 v^2 \nabla^2 p = -\mu_a \frac{\partial}{\partial t} I, \tag{3.4}$$

where k_0 is the thermal conductivity, ρ indicates the equilibrium density, $\mathrm{C_p}$ is the specific heat at constant pressure, βrepresents the expansion coefficient, v is the speed of sound in the medium, p indicates the acoustic pressure, μ_a is the absorption coefficient, I is the intensity of the laser pulse in the medium. By neglecting the effect of the acoustic wave on temperature and the diffusion of temperature in the Equation (3.4), temperature can be calculated,

$$\Delta T = \frac{\mu_a \varphi}{\rho C_p} \tag{3.5}$$

By substituting Equations (3.3) and (3.5) into Equation (3.2) and using $\Gamma = \frac{\beta c^2}{C_p}$, we find that

$$p = \Gamma \mu_a \varphi (1 + \frac{1}{\rho \beta c^2} \frac{\partial \Gamma}{\partial T} \mu_a \varphi) \tag{3.6}$$

The second term in Equation (3.6) represents nonlinearity due to light fluence (temperature). If we assume the second term is negligible, temperature rise is unlikely to explain the optoacoustic nonlinearity. By considering $\frac{\partial \Gamma}{\partial T} = 25 \times 10^{-4}\ (1/K)$ for water at room temperature [60] and under standard conditions for our phantom measurements ($\varphi = 10\ \mathrm{mJ/cm^2}$, $\mathrm{c} = 1480\ \mathrm{m}/s$, $\rho = 1000\ \mathrm{kg/m^3}$, and $\beta = 210 \times 10^{-6}\ 1/\mathrm{K}$ for water at room temperature, and $\mu_a = 0.1\ \mathrm{cm^{-1}}$), we have $\frac{1}{\rho \beta c^2} \frac{\partial \Gamma}{\partial T} \mu_a \varphi \approx 5.3 \times 10^{-6}$. Consequently, the second term in Equation (3.6) is negligible and

optoacoustic pressure is a linear function of fluence (temperature). However, the second term in Equation (3.6) has a singularity at $\beta = 0$. Therefore, the second term can have a significant value near the singularity and then the optoacoustic pressure is nonlinear as a function of fluence. For example, the thermal expansion of water becomes zero at $4\ ^{\circ}C$ [61, 62]. Therefore, the optoacoustic pressure might become nonlinear at low temperatures (close to $4\ ^{\circ}C$) for phantoms made of water. Therefore, we performed two experiments to investigate this hypothesis with a homogeneous agar cube phantom.

3.5.2 Phantom experiment

We initially performed an experiment to investigate the influence of temperature of the media on the optoacoustic pressure with a homogeneous agar cube with uniform absorption coefficient $\mu_a = 0.1\ \mathrm{cm}^{-1}$ and reduced scattering coefficient $\mu_s{}' = 4\ \mathrm{cm}^{-1}$ (3.2.2) which was illuminated at 5 mJ (800 nm) in transmission mode (Figure 3.1(a)). The temperature of the phantom was controlled, and the optoacoustic signal was acquired at five different temperatures 0.5, 2.5, 6.0, 10.80, and 17.0 degree Celsius. Figure 3.5a shows the maximum value of the optoacoustic signal as a function of the temperature of the media. According to Figure 3.5a, optoacoustic pressure is a linear function of temperature at a constant fluence.

Moreover, we performed another experiment to explore the nonlinear behavior of the optoacoustic signal as a function of fluence at different temperatures by controlling the temperature of the media.

In this experiment, we created a phantom of intralipid, pure water, ink, and agar, such that the reduced scattering coefficient was 4 cm^{-1} and absorption coefficient was $\mu_a = 0.1\ \mathrm{cm}^{-1}$ (See Sec. 3.2.2). Then the phantom was illuminated with different fluences at

different temperatures. Figure 3.5b shows the maximum of the optoacoustic signal as a function of light fluence at different temperatures. Figure 3.5b-c show that optoacoustic signals decrease with reducing temperature and become nonlinear at lower temperatures. Therefore, this observation is consistent with our theoretical results (Equation (3.6)), suggesting that optoacoustic pressure is nonlinear near the singularity ($4\ °C$ for water). In addition, since the phantom is made of both water and ink, the thermal expansion is not zero exactly at $4\ °C$. Consequently, the observed nonlinearity in our phantom measurements at room temperature cannot be explained by the laser-induced variations in temperature.

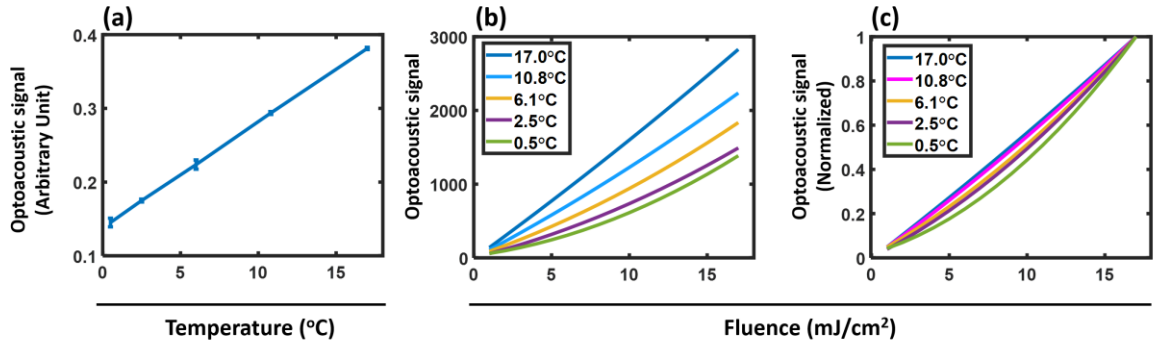

Figure 3.5. Exploring influence of temperature on optoacoustic pressure. A homogeneous agar cube with uniform absorption coefficient $\mu_a = 0.1\ cm^{-1}$ and reduced scattering coefficient $\mu_s' = 4\ cm^{-1}$ was illuminated at 10 mJ/cm^2 (800 nm) as a function of temperature. (a) Normalized maximum value of the acquired optoacoustic signal at light fluence 10 mJ/cm^2 as a function of temperature. (b) The maximum of the detected signal over light fluence at five different temperatures. (c) Normalization of the data in panel (b).

Moreover, we can approximately calculate the laser-induced local temperature rise in our phantoms. By using Equation (3.5) and under standard conditions for our phantom measurements ($\varphi = 10\ \mathrm{mJ/cm^2}$, $\rho = 1000\ \mathrm{kg/m^3}$ and $C_p = 4.18\ \mathrm{J/(gK)}$ for water, and $\mu_a = 0.1\ \mathrm{cm^{-1}}$), the light-induced changes in temperature is $\Delta T = 0.24\ \mathrm{mK}$, which is

generally too small to alter thermo-physical parameters of the sample sufficiently to induce nonlinearity.

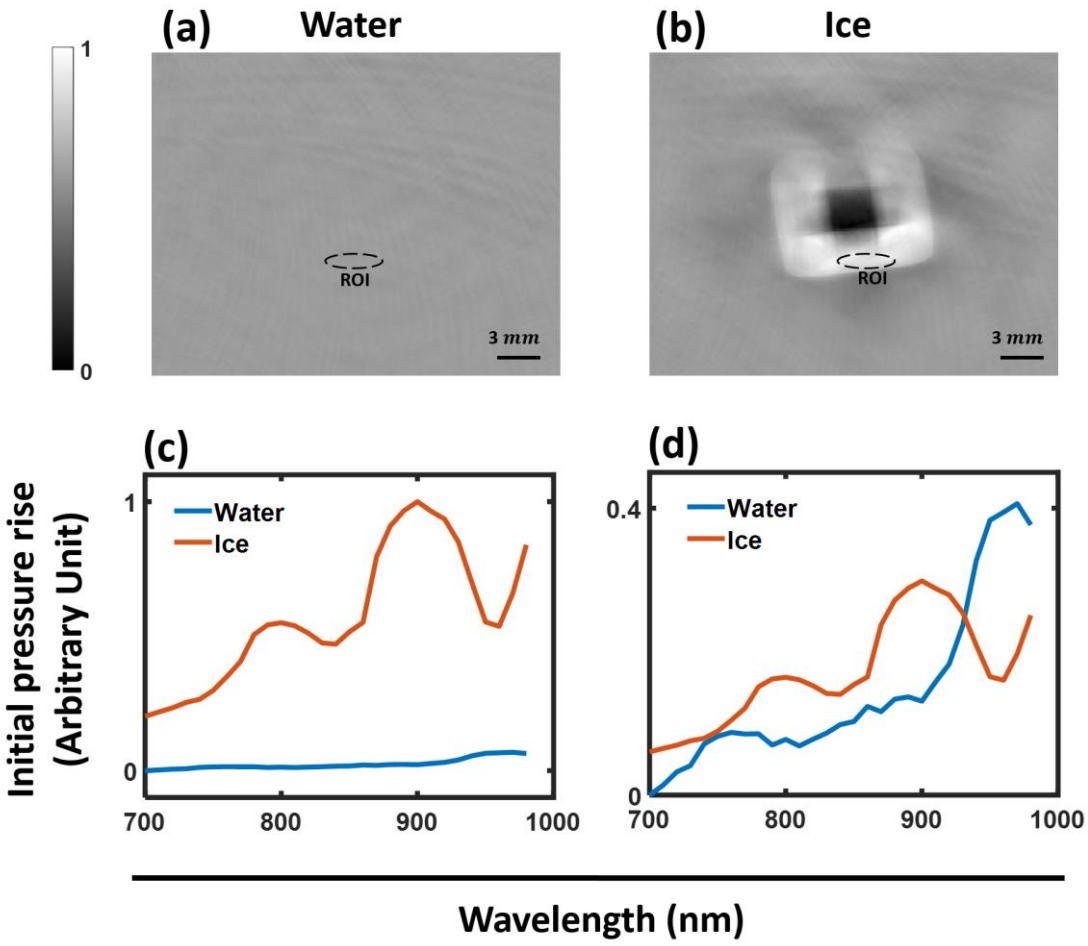

Figure 3.6. Optoacoustic spectra and reconstructed image of water and ice. Deionized water and an ice cube made of deionized water was illuminated over a wavelength range from 700 to 980 nm at a fluence about 4 $\mathrm{mJ/cm^2}$. (a) The distribution of initial pressure rise of deionized water based on the reconstruction of optoacoustic data acquired at a temperature of 20 degrees Celsius. (b) The distribution of initial pressure rise of the ice cube based on the reconstruction of the acquired optoacoustic data. (c) The optoacoustic spectra of water and ice according to the marked ROIs in panels (a) and (b). (d) Optoacoustic spectra of panel (c) normalized to the mean value.

3.6 Optoacoustic spectrum of ice

In this section, we investigated an unusual optoacoustic behavior of water at two different temperatures, below and above zero degrees Celsius. We measured the optoacoustic spectrum of water (above zero degrees Celsius) and ice (below zero degrees Celsius). We observed a significant discrepancy between the optoacoustic spectra and reconstructed image of liquid water and frozen water (ice). The optical absorptivity spectra of liquid water as a function of temperature has been explained [63]. Although optoacoustic spectra of liquid water and ice has been reported by using a resonant optoacoustic cell [64].

In this chapter by using multispectral optoacoustic tomography (MSOT), we showed, for the first time, the reconstructed image and spectrum of ice which is different from the previous work [64]. To show the discrepancy between the optoacoustic spectra and reconstructed image of water and ice over the wavelength range from 700 to 980 nm, the experiments were performed by using MSOT.

The measurements were performed on liquid and frozen deionized water. The optoacoustic signal of liquid water was acquired after filling the camber of the MSOT system (Figure setup) with deionized water at temperature of 20 degrees Celsius and the optoacoustic data was collected by illuminating the deionized water inside the chamber. To measure the optoacoustic signal of ice, we first prepared a cubic ice ($1 \times 1 \times 1\ cm$) using deionized water at temperature -20 degrees Celsius and then placed it in the center of the field of view of the array when the temperature of the chamber was about 0.5 degrees Celsius. In both measurements, the sample was illuminated over a wavelength range from 700 to 980 nm at a fluence of about 4 $\mathrm{mJ/cm^2}$, where the optoacoustic signal varies more or less linearly with fluence. To have an unchanged

temperature during the measurements, the acquisition time was about 10 seconds in each experiment.

Figure 3.6a and Figure 3.6b depict the distribution of the initial pressure rise of the deionized water and the ice cube respectively, after reconstructing the optoacoustic pressure obtained at laser wavelength 980 nm. Figure 3.6a and Figure 3.6b are normalized to the maximum value of Figure 3.6 b. Figure 3.6c shows the optoacoustic spectra of the deionized water and the cube ice, which is obtained by averaging the initial pressure rise at different wavelengths over the region of interests (ROI) marked in Figure 3.6a and Figure 3.6b. Figure 3.6d plots the spectra shown in Figure 3.6d normalized to the mean value.

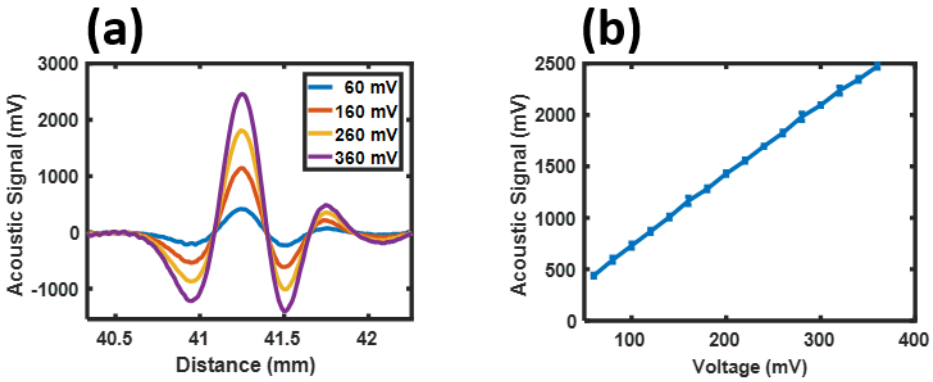

Figure 3.7. Testing the impact of the setup on the measurements. Using a transducer as the source of acoustic pressure as shown in Figure 3.2. (a) The detected acoustic signal by Transducer-2 at four different pulse signals as the input of Transducer-1. (b) The maximum of the detected acoustic signal as a function of the amplitude of the pulse signal.

3.7 Linearity of experimental setup

In this section, we examine the linear response of the used experimental setup. We initially modified the experimental setup (Figure 3.1a) by replacing the phantom by a

transducer as the source of the acoustic pressure. The modified setup is shown in Figure 3.2. Transducer-1 is a 3.5 MHz-flat transducer which operates as an acoustic source. Transducer-2 detects the generated acoustic signal. The input of Transducer-1 is a pulse signal with duty cycle 1 percent and frequency 50 kHz. Figure 3.7a shows the output of Transducer-2 (the detected acoustic signals) for four pulse signals (the input of Transducer-1) with different amplitudes. The maximum of the detected acoustic signal is plotted as a function of the amplitude of the pulse signal in Figure 3.7b. Figure 3.7b shows the detected acoustic signal is a linear function of the acoustic source. Therefore, the experimental setup used to investigate optoacoustic nonlinearity has a linear response and the observed nonlinearity in our measurements is not caused by the experimental setup.

3.8 Discussion

We improved the previous experimental setup (Figure 2.1) by using tomographic samples, a transmission mode setup (Figure 3.1(a)), and cubic phantoms. By applying these three alterations and acquiring a simple bipolar optoacoustic signal, we confirmed that the nonlinearity cannot be explained by variations of fluence as a function of depth. This observation implies that the local temperature rise might not cause the nonlinearity in optoacoustic signal and the observed nonlinearity should be explained by other phenomena. We test this idea by calculating the width of the phantom using the distance between the first and second front of the optoacoustic signal observed with an agar cube phantom (Figure 3.3a and Figure 3.3b) at different fluence. We found that the width of the phantom shrinks with increasing fluence. This is the opposite of the "expansion" we would expect if temperature changes were causing the nonlinear response. Therefore, we theoretically and experimentally

explored the influence of temperature on the optoacoustic pressure. We presented the optoacoustic pressure by considering Grueneisen parameter as a nonlinear function of temperature. We found a singularity in the nonlinear term of the derived equation. The singularity happens when the thermal expansion becomes zero. Therefore, the nonlinear term is not negligible at a certain temperature wherein the thermal expansion becomes zero. Our experimental results showed that optoacoustic pressure is linear at room temperature and becomes more nonlinear at low temperatures. This is consistent with our theoretical results, suggesting that the optoacoustic signal is more nonlinear at low temperatures (close to singularity). Therefore, the local temperature rise may not be a major contributor in the observed nonlinearity at room temperature.

In the last section of this chapter, we showed that there is a significant difference between optoacoustic behavior of liquid water and frozen water (ice). We observed that the detected optoacoustic pressure from an ice cube is much stronger than that of water. Furthermore, the optoacoustic spectra of ice and water are completely different.

4 Electro-optoacoustic pressure contributes to nonlinearity in optoacoustics

4.1 Introduction

The signals recorded in optoacoustic sensing or imaging exhibit nonlinear effects at illuminations above 6 mJ/cm2 [65]. Nonlinear effects have been observed both in optical resolution optoacoustic microscopy, which uses focused light for signal excitation, and in acoustic-resolution optoacoustic imaging that uses broad-beam illumination [39, 40, 42, 43]. We have further shown that the nonlinear behavior depends on the wavelength employed and the properties of the sample [65]. The presence of nonlinear effects has implications for the accuracy of optoacoustic measurements in spectroscopic or imaging applications. Generally, optoacoustic imaging methods do not take these effects into account but assume that optoacoustic

signal intensity is proportional to the illuminating fluence [16] [20]. Nevertheless, not accounting for nonlinearity at higher light fluences may lead to erroneous estimates of chromophore concentrations or readings of tissue pathophysiology.

While the presence of nonlinear signals has been confirmed in many optoacoustic studies, the origin of the nonlinear optoacoustic signal remains unclear. Previous work suggested that the nonlinear behavior may be due to a local temperature rise in the sample, which leads to changes in thermo-physical parameters, such as the Grüneisen parameter [43], ultimately altering the acoustic properties of the sample and the recorded signal. Likewise, other studies have suggested that the local temperature rise may induce material phase effects, such as fluid evaporation or nano-bubble formation leading to nonlinear signal amplification [39, 40]. Nonlinearity at high fluences has also been explained through saturation of the absorption coefficient [42]. Although temperature rise may be implicated in the generation of optoacoustic nonlinearity, especially at high illumination fluences, it is unclear whether moderate fluences (<20 mJ/cm2) employed in biomedical measurements generate nonlinearity through temperature effects. The instantaneous temperature rise from pulsed light sources at moderate fluence is on the order of milli-Kelvins [66]. Such temperature rise is unlikely to form nano-bubbles [40]. Moreover, the relation between Grüneisen parameter variations and nonlinearity is not clearly established.

In this chapter, we theoretically and experimentally investigated alternative possible causes of optoacoustic nonlinearity at moderated light fluences (<20 mJ/cm2). Our results indicate thermally excited nonlinear susceptibility as a major contributor of optoacoustic nonlinear behavior. We observed variations in the shape of optoacoustic signal acquired from the phantoms with moderate absorption coefficient by increasing fluence which cannot be explained with temperature rise. Therefore, we obtained the

general pressure wave equation by investigating the light-induced changes in a dielectric slab. We theoretically showed thermally excited changes in the dielectric constant generates an additional acoustic pressure called electro-optoacoustic pressure which causes nonlinearity in the acquired optoacoustic signal and can be observed better in the high frequency component of the measured signal. By phantom measurement, we measured the nonlinear variation in the acquired optoacoustic signal over light fluence in both the frequency and time domain.

Based on these results, we initially extracted the electro-optoacoustic pressure from the total optoacoustic pressure and then we developed an algorithm to reconstruct an image from the electro-optoacoustic pressure. The reconstructed image indicates thermally excited third-order nonlinear susceptibility as a contrast mechanism. Further optimization of this algorithm and validation in more samples may provide a highly useful tool in optoacoustic tomography. Our results may also have important implications for nonlinear behavior in optoacoustic micro- and mesoscopy.

4.2 Methods

4.2.1 Phantoms

Tissue-mimicking homogeneous phantoms (analyzed in Figure 4.2 and Figure 4.3) were prepared as cubes (1 x 1 x 1 cm) by mixing agar (2% solution in deionized water, 05039-500G, Sigma-Aldrich, Steinheim, Germany) with black India ink (Higgins, Texas) and intralipid (20% emulsion, I141-100ML, Sigma). The ink was first diluted using deionized water as needed in order to obtain the desired final absorption coefficients, as determined using a spectrometer (LS-1-cal, USB4000; Ocean Optics, Germany). The amount of intralipid was also varied in order to achieve different reduced scattering

coefficients [51]. First, the ink and intralipid were mixed, then the 2% agar was added, and the entire mixture was heated in a microwave oven.

4.2.2 Optoacoustic data acquisition

To investigate the electro-optoacoustic phenomenon in phantoms, the results of which are shown in Figure 4.2 and Figure 4.3 we used the experimental setup shown in Figure 3.1a. Each phantom was produced three times and each measurement was performed three times for each phantom.

To examine the electro-optoacoustic pressure extracted from measured optoacoustic pressure of the mouse kidney cross-section, the results of which are shown in Figure 4.4, a small-animal multispectral optoacoustic tomography scanner (MSOT256-TF; iThera Medical, Germany) and imaging setup shown in Figure 3.1b were used.

4.3 Theory

4.3.1 Optoacoustic pressure

This chapter investigated all possible sources that could contribute to the generated optoacoustic pressure, hence we initially investigated the effects of the electric field on an absorptive dielectric media. We consider a dielectric slab between a parallel plate capacitor as shown in Figure 4.1. The dielectric slab has a relative permittivity of ε, a refractive index of $n = \sqrt{\varepsilon}$ and an absorption coefficient of μ_a (assuming the material is non-magnetic). The electric field strength between the parallel-plate capacitor is E. When, the dielectric slab is located between the capacitor plates, the potential energy per unit volume of the dielectric slab is given as,

$$u = \frac{1}{2}\varepsilon_0 \varepsilon E^2 \tag{4.1}$$

where, $\boldsymbol{\varepsilon_0}$ is vacuum permittivity. The heat generated per unit volume in the dielectric slab is,

$$\Delta Q = \mu_a \int I dt \tag{4.2}$$

where, $I = \varepsilon_0 ncE^2$ is field intensity [67]. In the consideration of thermal effects, energy is the relevant quantity for pulsed lasers [67].

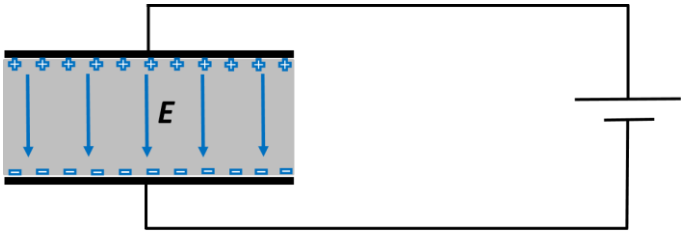

Figure 4.1. A dielectric slab located between a parallel-plate capacitor. *E* is the electric field strength between the plates.

The second law of thermodynamics is given as,

$$T\Delta s = \Delta QV \tag{4.3}$$

where s is the entropy, T indicates the temperature and V represents the volume. Further the change in the entropy is given by $\Delta s = \left(\frac{\partial s}{\partial T}\right)_p \Delta T$, where the change in entropy versus temperature at constant pressure (p) can be obtained using Maxwell relations, which is given as,

$$\left(\frac{\partial s}{\partial T}\right)_p = \frac{\rho C_p}{T} \tag{4.4}$$

where C_p represents specific heat capacity and ρ indicates the mass density. Now the change in the temperature of the dielectric slab induced by the generated heat per unit of volume (Q) is given by (using Equations (4.3) and (4.4)),

$$\Delta T = \frac{\mu_a \varphi}{\rho C_p} \tag{4.5}$$

where, $\varphi = \int \mathrm{I(t)dt}$ is light fluence. Next the change in pressure versus temperature at constant volume can be written as,

$$\Delta p = \left(\frac{\partial p}{\partial T}\right)_V \Delta T \tag{4.6}$$

Further using Maxwell relations, we can also represent the change in pressure versus temperature at constant volume in terms of thermal expansion coefficient, which is given as,

$$\left(\frac{\partial p}{\partial T}\right)_V = \beta \rho v^2 \tag{4.7}$$

where, v is speed of sound, and β is the thermal expansion at constant pressure. Now the thermally excited pressure by the transferred heat can be estimated by substituting Equations (4.5) and (4.7) into Equation (4.6),

$$\Delta p = \frac{\beta v^2}{C_p} \mu_a \varphi \tag{4.8}$$

By introducing Grueneisen parameter ($\Gamma = \frac{\beta v^2}{C_p}$) and $\Delta p = p_{th}$ as thermally excited pressure into Equation (4.8), we can obtain

$$p_{th} = \Gamma \mu_a \varphi \tag{4.9}$$

4.3.2 Electro-optoacoustic pressure

We investigated the variation in the field energy density (Equation (4.1)) of the dielectric slab (Figure 4.1) due to the change in temperature and pressure (Equations (4.5) and (4.8)). By considering density and temperature as two independent thermodynamic variables, the changes in the relative permittivity induced by light intensity can be represented by,

$$\Delta\varepsilon = \left(\frac{\partial\varepsilon}{\partial\rho}\right)_T \Delta\rho + \left(\frac{\partial\varepsilon}{\partial T}\right)_\rho \Delta T \tag{4.10}$$

where, the first term represents the change in the dielectric constant versus density at constant temperature and the second term represents the change in the dielectric constant versus temperature at constant density. Therefore, the potential energy density (Equation (4.1)) changes by the amount,

$$\Delta u = \frac{1}{2}\varepsilon_0 \Delta\varepsilon_{th} E^2 \tag{4.11}$$

Assuming that no external energy is added, according to the first law of thermodynamics at constant temperature, the change in energy (Equation (4.11)) equals to the work performed on the system (dielectric slab) which is given by,

$$\frac{\Delta w}{V} = \frac{\Delta pV}{V} = \Delta u \tag{4.12}$$

where, Δw is change in work at constant volume. By introducing Equation (4.11) for the energy density into Equation (4.12) and using $I = \varepsilon_0 ncE^2$, the excited pressure by Δp is given by,

$$p_{eo} = \frac{\Delta\varepsilon_{th}}{2nc} I \tag{4.13}$$

We named $\Delta p = p_{eo}$ as electro-optoacoustic pressure which is due to thermally excited change in the dielectric constant (refractive index).

4.3.3 The total acoustic wave equation

We showed the dielectric slab (Figure 4.1) experience the contribution of the two different pressures and the total pressure is given by,

$$p_{tot} = p_{th} + p_{eo} = \Gamma\mu_a\varphi + \frac{\Delta\varepsilon_{th}}{2nc} I \tag{4.14}$$

By replacing φ with $\int \mathrm{I(t)dt}$, the electro-optoacoustic pressure is proportional to the derivative of thermal pressure,

$$p_{eo} \propto \frac{\partial p_{th}}{\partial t} \tag{4.15}$$

To investigate the effects of the total pressure (p_{tot}) in optoacoustic imaging, we derived acoustic pressure wave equation by using Navier-Stokes and continuity equations [68-72],

$$\rho\left[\frac{\partial \vec{v}}{\partial t} + (\vec{v}\cdot\nabla)\vec{v}\right] = -\nabla p + F + \eta_s \nabla^2 \vec{v} + (\eta_b + \frac{1}{3}\eta_s)\nabla(\nabla.\vec{v}) \tag{4.16}$$

$$\frac{\partial \rho}{\partial t} + \nabla.(\rho\vec{v}) = 0 \tag{4.17}$$

where, $\vec{v}$ is velocity vector; η_s and η_b are shear and bulk viscosity, respectively; F represents the force per unit volume which is given by

$$F = -\nabla p_{tot} = -\Gamma\mu_a \nabla\varphi - \frac{\Delta\varepsilon_{th}}{2nc}\nabla I \tag{4.18}$$

By neglecting the convective acceleration term and the viscosity effects in Equation (4.16) and using Equation (4.18), we find

$$\rho\frac{\partial \vec{v}}{\partial t} = -\nabla p - \Gamma\mu_a \nabla\varphi - \frac{\Delta\varepsilon_{th}}{2nc}\nabla I \tag{4.19}$$

After differentiating Equation (4.17) with respect to time and applying the divergence on (4.19), we find that

$$\nabla.\left(\rho\frac{\partial \vec{v}}{\partial t}\right) = -\frac{\partial^2 \rho}{\partial t^2} \tag{4.20}$$

$$\nabla.(\rho\frac{\partial\vec{v}}{\partial t}) = -\nabla^2 p - \Gamma\mu_a\nabla^2\varphi - \frac{\Delta\varepsilon_{th}}{2nc}\nabla^2 I \tag{4.21}$$

By substituting Equation (4.20) into Equation (4.21) and using $\frac{\partial p}{\partial \rho} = v^2$, we find that

$$\nabla^2 p(r,t) - \frac{1}{v^2}\frac{\partial^2}{\partial t^2}p(r,t) = -\frac{\Gamma\mu_a}{v^2}\frac{\partial}{\partial t}I(r,t) - \frac{\gamma_e}{2ncv^2}\frac{\partial^2}{\partial t^2}I(r,t) \tag{4.22}$$

where, $\gamma_e = \Delta\varepsilon_{th}$ is electro-optoacoustic constant and v is the speed of sound; the spatial derivatives were replaced by time derivative by using $r = vt$ and the term $\nabla^2\varphi$ was written as $\frac{1}{v^2}\frac{\partial \mathrm{I}}{\partial \mathrm{t}}$ by replacing $\varphi = \int \mathrm{I(t)dt}$. The first and second terms in the right-hand side of Equation (4.22) are the source terms of the thermal and electro-optoacoustic pressure, respectively.

The change in the dielectric constant can be related to the nonlinear susceptibility by [67],

$$\Delta\varepsilon_{th} = \frac{\chi_{th}^{(3)} I}{n\varepsilon_0 c} \tag{4.23}$$

where, $\chi_{th}^{(3)}$ is the third-order nonlinear optical susceptibility due to thermal effects and with roughly the typical value of $10^{-12}\ m^2/V^2$ [67]. By approximating $\varphi \approx \mathrm{I}\Delta\mathrm{t}$ and Equations (4.14) and (4.23), the calculated initial pressure rise from Equation (4.22) can be written as,

$$p_{tot} = p_{th} + p_{eo} = \Gamma\mu_a\Delta t\ I\ + \frac{\chi_{th}^{(3)}}{2\varepsilon_0(nc)^2}I^2 \tag{4.24}$$

where, Δt is the laser pulse duration. Equation (4.24) shows the thermal and electro-optoacoustic pressures behave linear and nonlinear with light energy, respectively. Moreover, the measured optoacoustic pressure in a measurement includes both

thermal and electro-optoacoustic pressures which should be unmixed (section 4.4.2). According to the nonlinear behavior of electro-optoacoustic pressure, we can extract the electro-optoacoustic pressure from the measured total pressure (p_{tot}). Since the thermal pressure (p_{th}) is linear, the electro-optoacoustic pressure (p_{eo}) can be obtained from the subtraction of two normalized total optoacoustic pressure measured at two different light intensities. By using Equation (4.24), we find that

$$\Delta\tilde{p}_{tot} = \frac{p_{tot2}}{I_2} - \frac{p_{tot1}}{I_1} = \frac{\chi_{th}^{(3)}}{2\varepsilon_0(nc)^2}\Delta I \tag{4.25}$$

where, p_{toti} is the total optoacoustic pressure at fluence I_i; ΔI is $I_2 - I_1$. Equation (4.25) represents $\Delta\tilde{p}_{tot}$ equals to the normalization of the electro-optoacoustic pressure when light intensity is ΔI. Then, we can obtain,

$$\Delta\tilde{p}_{tot} \propto \tilde{p}_{eo} = \frac{p_{eo}}{I} \tag{4.26}$$

where, $\tilde{p}_{eo}$ is the normalization of p_{eo}. Therefore, the thermally excited third-order nonlinear susceptibility can be estimated to be,

$$\chi_{th}^{(3)} = n\varepsilon_0 c\frac{\Delta\tilde{p}_{tot}}{\Delta I} \tag{4.27}$$

Standard optoacoustic image reconstruction algorithms assume that the measured overall signal (p_{tot}) is equivalent to the thermal pressure (p_{th}). However, these theoretical considerations led us to hypothesize the effects of electro-optoacoustic pressure may be significant in a measured optoacoustic signal. Therefore, we investigated experimentally whether electro-optoacoustic pressure contributes significantly to the measured optoacoustic signal. If electro-optoacoustic pressure contribution is significant, we can improve the measured data by removing the electro-

optoacoustic pressure and also obtain thermally excited third-order nonlinear susceptibility ($\chi_{th}^{(3)}$) as a new parameter of the sample as well as absorption coefficient. Our investigation regarded conditions typically used in biomedical optoacoustic imaging.

4.4 Results

In this section, we experimentally verified the theoretical description of the optoacoustic pressure presented in the previous section. The existence and effects of the electro-optoacoustic pressure was investigated in both frequency and time domains. In section 4.4.1, the optoacoustic pressure wave equation was solved in the frequency domain and the data collected from a tissue-mimicking phantom was analyzed in the frequency domain to validate our theoretical results. The existence of the electro-optoacoustic signal was also investigated in the time domain in section 4.4.2. In section 4.4.3, we tried to reconstruct an electro-optoacoustic image by calculating the electro-optoacoustic pressure of an in-vivo dataset.

4.4.1 Frequency domain

Our theoretical considerations indicated that there may be other pressures than the thermal pressure that could contribute to the measured optoacoustic pressure. In order to better understand other pressures contributing to the measured optoacoustic pressure, we solved the general form of the pressure wave equation (Equation (4.22)) for a symmetric cylindrical coordinate system along the z axis that was also experimentally investigated using phantoms (Figure 3.1a). The changes in the light intensity as a function of z can be approximated as an exponential decay in the z-direction, with no changes in the radial direction which is given by,

$$I(z,t) = I_0 I_z I_t = I_0 exp(-\mu_{eff} z - 4\frac{t^2}{t_0^2}) \tag{4.28}$$

where, $I_z = \exp(-\mu_{eff}\mathrm{z})$ and $I_t = \exp(-4\frac{\mathrm{t}^2}{\mathrm{t}_0^2})$. The pressure wave (p) generated by the laser intensity I are given by Equation (4.22). The general solution of the pressure equation wave can be obtained by taking the Fourier transform of both the sides of Equation (4.22):

$$\nabla^2 \tilde{p}(z,\omega) + k^2 \tilde{p}(z,\omega) = S(z,\omega) \tag{4.29}$$

where $\tilde{\mathrm{p}}$ is the Fourier transform of p and $S(\mathrm{z},\omega)$ is the source term which is given by,

$$S(z,\omega) = I_0 I_\omega I_z(-iA + B) \tag{4.30}$$

where I_ω is the Fourier transform of I_t, $\mathrm{A} = \frac{\Gamma\mu_a}{v^2}\omega$ and $\mathrm{B} = \frac{\gamma_e}{2\mathrm{nc}}k^2$; where $\mathrm{k} = \frac{\omega}{\mathrm{v}}$. Equation (4.29) can be solved by using Green's function in cylindrical coordinates and only in the z direction. The boundary condition for the wave equation, which is describing a wave traveling in both directions along the z axis, is $\mathrm{z} \in (-\infty, \infty)$. Equation (4.29) is a Sturm-Liouville problem of the third kind (SLP3) due to infinite boundary conditions. Therefore, the solution is given by

$$\tilde{p}(z',\omega) = \int_{-\infty}^{+\infty} S(z,\omega) g(z,z') dz, \tag{4.31}$$

where $\mathrm{g}(\mathrm{z},\mathrm{z}')$ is Green's function (one dimension) given by,

$$g(z,z') = \frac{e^{-ik|z-z'|}}{2ik}, \tag{4.32}$$

Therefore, the solution can be written:

$$\tilde{p}\left(z^{'},\omega\right)=\frac{I_0 I_\omega}{2k}\left[(-A-iB)I_1^{'}\right]e^{-ikz^{'}}+\frac{I_0 I_\omega}{2k}[(-A-iB)I_1]e^{ikz^{'}}, \quad (4.33)$$

where $\mathrm{I}_1'=\int_{-\infty}^{\mathrm{z}'}\mathrm{I_z}\exp(\mathrm{ikz})\,\mathrm{dz}$ and $\mathrm{I}_1=\int_{\mathrm{z}'}^{+\infty}\mathrm{I_z}\exp(-\mathrm{ikz})\,\mathrm{dz}$. Then, $\tilde{\mathrm{p}}(\mathrm{z},\omega)$ can be rewritten by changing z' to z:

$$\tilde{p}(z,\omega)=\tilde{p}^{+}(z,\omega)+\tilde{p}^{-}(z,\omega), \quad (4.34)$$

$$\tilde{p}^{+}(z,\omega)=-\frac{I_0 I_\omega I_1^{'}}{2k}(A+iB)exp(-ikz) \quad (4.35)$$

$$\tilde{p}^{-}(z,\omega)=-\frac{I_0 I_\omega I_1}{2k}(A+iB)exp(ikz) \quad (4.36)$$

In Equation (4.34), the first term $\tilde{\mathrm{p}}^{+}(\mathrm{z},\omega)$ is a wave traveling in the positive z direction and the second term $\tilde{\mathrm{p}}^{-}(\mathrm{z},\omega)$ is a wave traveling in the negative direction. If an acoustic detector (transducer) is placed at position z<0, the detected acoustic signal would be $\tilde{\mathrm{p}}^{-}(\mathrm{z},\omega)$, which includes both thermal and electro-optoacoustic pressure:

$$\tilde{p}_{th}^{-}(z,\omega)=M_1 I_0 \quad (4.37)$$

$$\tilde{p}_{eo}^{-}(z,\omega)=M_2 I_0^2\omega \quad (4.38)$$

where, $\tilde{p}_{th}^{-}$ and $\tilde{p}_{eo}^{-}$ are thermal and electro-optoacoustic pressure, respectively; $M_1=-\frac{\mathrm{I}_\omega \mathrm{I}_1}{2v}\Gamma\mu_a\exp(\mathrm{ikz})$ and $M_2=-i\frac{I_\omega I_1}{2v}\frac{\chi_{th}^{(3)}}{2\varepsilon_0(nc)^2}exp(ikz)$. For simplicity, we considered γ_e as a function of I_0 instead of I. By calculating the absolute ratio between electro-optoacoustic and thermal pressures, we can find

$$R=\left|\frac{\tilde{p}_{eo}^{-}}{\tilde{p}_{th}^{-}}\right|=\frac{\chi_{th}^{(3)}}{2\varepsilon_0(nc)^2\Gamma\mu_a}\omega I \quad (4.39)$$

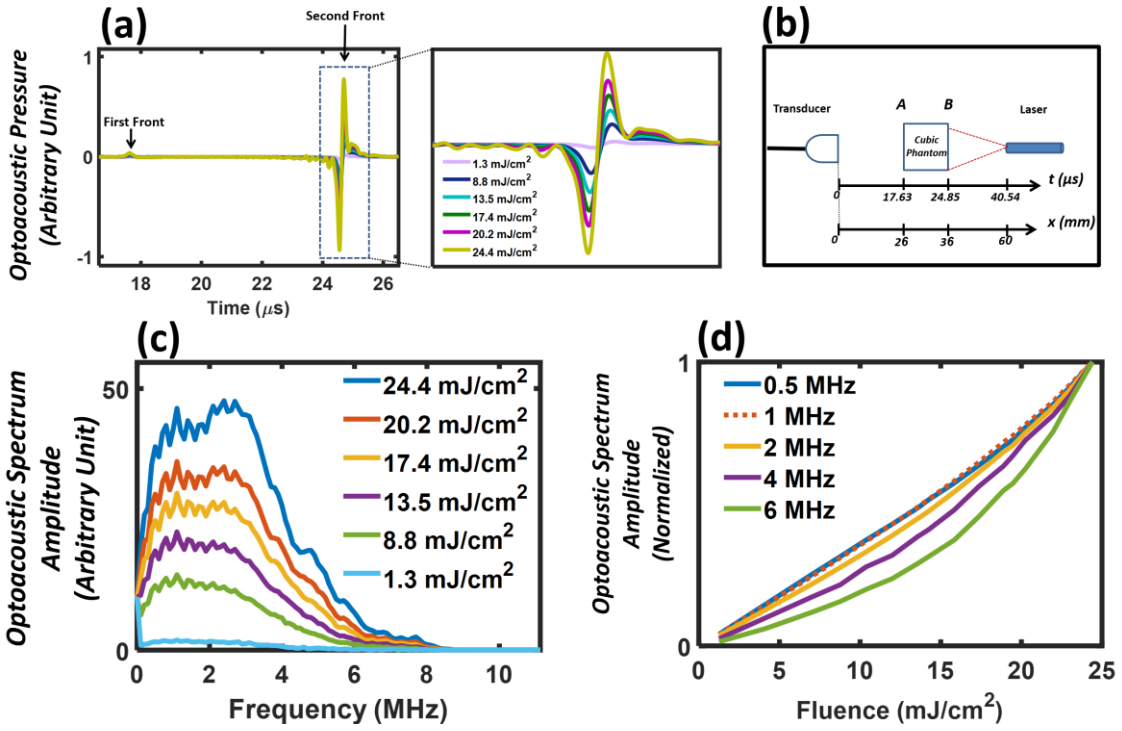

Figure 4.2. Changes in the optoacoustic spectrum and signal as a function of fluence. A homogeneous agar cube with uniform reduced scattering coefficient $\mu_s' = 4\ \mathrm{cm}^{-1}$ and absorption coefficient $\mu_a = 0.1\ \mathrm{cm}^{-1}$ was illuminated with a laser operating at 800 nm with different fluence levels on the sample. (a) Raw optoacoustic data. Signals corresponding to the first edge (closer to transducer) or second edge (closer to illumination source) are labelled. The inset plot shows the signal from the second edge in greater detail. (b) Phantom location in the setup base on time and distance axis. (c) The spectra of the signals in panel (a). (d) The optoacoustic spectrum amplitude at different frequencies as a function of fluence.

The relationships in Equations (4.37)-(4.39) can be tested experimentally in order to determine whether electro-optoacoustic pressure contributes to the optoacoustic measurements. Equations (4.37) and (4.38) imply that the amplitude of thermal pressure is a linear function of light intensity and independent of frequency (ω) but the electro-optoacoustic pressure is a second-degree polynomial function of light intensity and a linear frequency-dependent pressure. Therefore, the contribution of the electro-

optoacoustic pressure should become more significant at higher frequencies. Consequently, the nonlinearity of the measured optoacoustic pressure should become stronger at higher frequencies.

Therefore, we examined and characterized the existence of the electro-optoacoustic signal as a function of light fluence by using Equations (4.37)-(4.39). We assessed the behavior of the detected optoacoustic signal from an optically diffusive phantom at different fluence. A homogeneous agar cube with uniform absorption coefficient $\mu_a = 0.1\ \mathrm{cm}^{-1}$ and reduced scattering coefficient $\mu_s' = 4\ \mathrm{cm}^{-1}$ was illuminated with various fluences at 800 nm in transmission mode. The resulting optoacoustic signals featured a first rising front corresponding to the pressure generated in the part of the cube closer to the transducer (edge A), followed by a second front corresponding to the pressure generated in the part closer to the illumination source (edge B; Figure 4.2a and b). The signal at the first front was relatively weak due to light attenuation through the phantom, whereby the signal at the second front was stronger, as it was illuminated with a non-attenuated fluence. We next calculate the Fourier transform of each measured optoacoustic signal at different light fluence (Figure 4.2c). Figure 4.2d shows the optoacoustic spectrum amplitude as a function of fluence at different frequencies. The optoacoustic spectrum amplitude become more nonlinear at higher frequencies which is consistent with Equations (4.37) and (4.38). At higher frequencies, the contribution of the electro-optoacoustic pressure, which is a nonlinear pressure, becomes more significant. The electro-optoacoustic signal contribution is negligible for the frequency components less than 1 MHz which are roughly linear (Figure 4.2d). We can interpret the observed nonlinearity (Figure 4.2d) as the nonlinearity due to the electro-optoacoustic pressure. If the observed nonlinearity (Figure 4.2d) is caused by the

thermal pressure (temperature), we should be able to see the nonlinearity in all of the frequency components, which is inconsistent with our observations (Figure 4.2d).

4.4.2 Time domain

In this section, we analyzed the influence of the electro-optoacoustic pressure on the measured optoacoustic signals, in the time domain, by using the theoretical description of the electro-optoacoustic pressure in section 4.3.3. We used the collected data shown in Figure 4.2a. We first choose measured signals at minimum fluence ($1.3\,\frac{\mathrm{mJ}}{\mathrm{cm^2}}$) and maximum fluence ($24.2\,\frac{\mathrm{mJ}}{\mathrm{cm^2}}$) which were normalized by the corresponding fluence and labeled $\hat{p}_{min} = \frac{p_{min}}{I_{min}}$ and $\hat{p}_{max} = \frac{p_{max}}{I_{max}}$ (Figure 4.3a). If the total pressure includes only the linear thermal pressure, $\hat{p}_{min}$ and $\hat{p}_{max}$ should fit each other very well. However, Figure 4.3a shows $\hat{p}_{min}$ and $\hat{p}_{max}$ are different in both phase and amplitude. Therefore, the measured optoacoustic signal behaves nonlinearly which cannot be due to temperature variations as mentioned in section 4.4.1. We can assume the observed nonlinearity is due to the electro-optoacoustic pressure which can be extracted from the total measured optoacoustic pressure by using Equation (4.25). By substituting p_{min} and p_{max} as $p_{tot1}$and p_{tot2}, respectively, into Equation (4.25), we find that

$$\Delta\tilde{p}_{tot} = \hat{p}_{max} - \hat{p}_{min} = \frac{\chi_{th}^{(3)}}{2\varepsilon_0(nc)^2}\Delta I \tag{4.40}$$

where, ΔI is $I_{\max} - I_{\min}$. By using Equations (4.26) and (4.40), we find that

$$\Delta\tilde{p}_{tot} = \frac{p_{eo}}{\Delta I} \tag{4.41}$$

where p_{eo} is the electro-optoacoustic pressure, when light intensity is ΔI. Figure 4.3b shows $\Delta\tilde{p}_{tot}$ which is calculated using Equation (4.40). To evaluate our assumption,

we can use Equations (4.15) and (4.26) which gives $\Delta\tilde{p}_{tot}$; which is proportional to the derivative of the thermal pressure,

$$\Delta\tilde{p}_{tot} \propto \frac{\partial p_{th}}{\partial t} \tag{4.42}$$

Since the electro-optoacoustic pressure is nonlinear with respect to the light fluence (Equation (4.24)), the contribution of electro-optoacoustic pressure in the measured optoacoustic signal at low fluences (p_{min}) can be neglected. Therefore, we can approximately replace the thermal pressure (p_{th}) by $\hat{p}_{min}$ in Equation (4.42), in which case we find from Equation (4.42) that,

$$\frac{\Delta\tilde{p}_{tot}}{|\Delta\tilde{p}_{tot}|} \cong \frac{\frac{\partial p_{min}}{\partial t}}{\left|\frac{\partial p_{min}}{\partial t}\right|} \tag{4.43}$$

A proof of the validity of Equation (4.43) verifies our assumption; the observed nonlinearity is due to the electro-optoacoustic pressure. Figure 4.3c shows the normalization of both $\frac{\partial p_{min}}{\partial \mathrm{t}}$ and $\Delta\tilde{p}_{tot}$ which fit each other very well as the validity of Equation (4.43). This proves the existence of electro-optoacoustic pressure and its behavior being nonlinear.

Since the electro-optoacoustic pressure is a second-degree polynomial function of light intensity (Equation (4.24)), $\Delta\tilde{p}_{tot}$ as the normalization of the electro-optoacoustic pressure (Equation (4.41)) should be a linear function of light intensity (Equations (4.25) and (4.40)). Therefore, we can prove the electro-optoacoustic pressure behaves nonlinearly by showing that $\Delta\tilde{p}_{tot}$ is a linear function of light intensity (ΔI). To calculate $\Delta\tilde{p}_{tot}$ at different fluences, we subtract $\hat{p}_{min}$ from all of the measured optoacoustic signals at different fluence which are normalized to the corresponding fluences (Figure 4.3d). Figure 4.3e shows the maximum value of each $\Delta\tilde{p}_{tot}$ shown in Figure 4.3d, as a

function of fluence and a linear function fitting. Since the maximum value of $\Delta\tilde{p}_{tot}$ is approximately linear over fluence (Figure 4.3e), we can then consider the electro-optoacoustic pressure as a second-degree polynomial function of fluence which is consistent with the theory (Equation (4.25) and (4.40)).

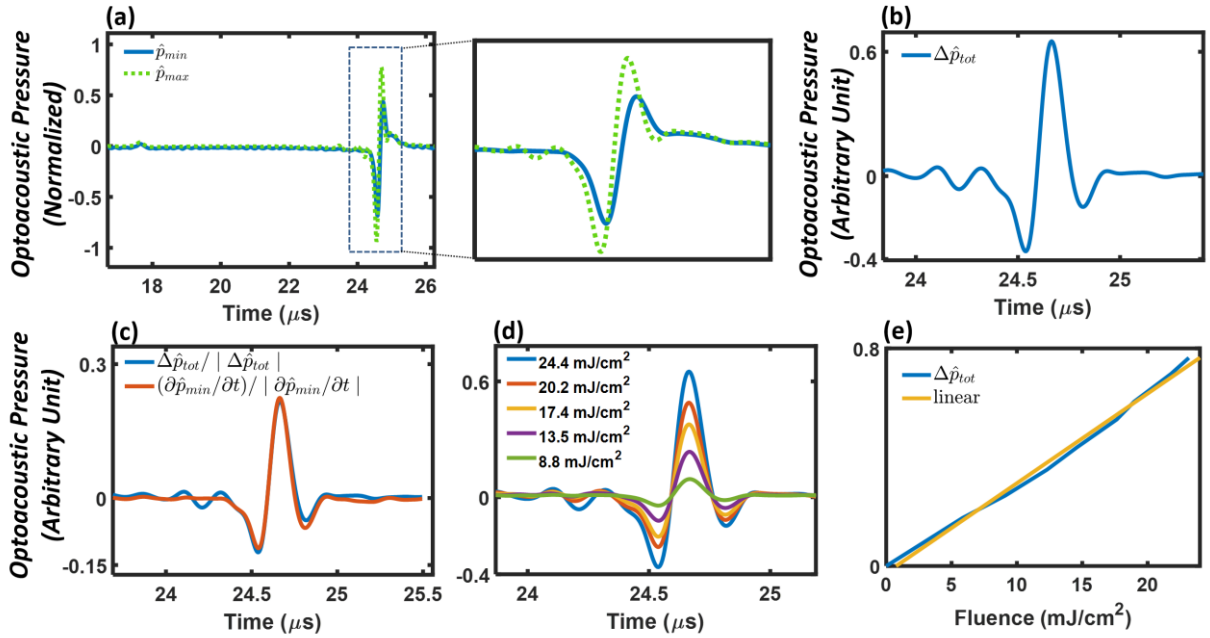

Figure 4.3. Exploring the electro-optoacoustic pressure as a function of fluence. In panels (a)-(e), a homogeneous agar cube with uniform absorption coefficient $\mu_a = 0.1\ \mathrm{cm}^{-1}$ and reduced scattering coefficient $\mu_s' = 4\ \mathrm{cm}^{-1}$ was illuminated with laser operating at 800 nm with different fluence levels on the sample (a) $\hat{p}_{min}$ and $\hat{p}_{max}$ are the optoacoustic signal at fluence 1.3 and 24.4 mJ/cm2, respectively, which are normalized to the corresponding fluence. (b) $\Delta\tilde{p}_{tot}$ as the result of subtracting $\hat{p}_{min}$ from $\hat{p}_{max}$. (c) The similarity of $\Delta\tilde{p}_{tot}$ and $\frac{\partial p_{min}}{\partial t}$ as $\frac{\partial p_{th}}{\partial t}$ after normalization. (d) The calculated $\Delta\tilde{p}_{tot}$ for different fluences by subtracting $\hat{p}_{min}$ from the optoacoustic signals normalized by the corresponding fluences. (e) The maximum value of calculated $\Delta\tilde{p}_{tot}$ in panel (d) over the variation of the corresponding fluence with respect to the minimum fluence (1.3 mJ/cm2) and a linear function fitting.

4.4.3 Electro-optoacoustic imaging

We showed that the electro-optoacoustic pressure can influence the measured optoacoustic signal in a nonlinear manner. This observation implies that the electro-optoacoustic pressure reflects a new contrast mechanism relating to the thermally excited third-order nonlinear susceptibility ($\chi_{th}^{(3)}$) of tissues. To produce images of $\chi_{th}^{(3)}$ contrast by using electro-optoacoustic pressure, we developed an image reconstruction algorithm. By using Poisson-type integral, the analytical solution of Equation (4.22) is given by,

$$p(r,t) = N_1 \frac{\partial}{\partial t} \int_{l(t)} \frac{\mu_a I}{|r-r'|} dl(t) + N_2 \frac{\partial^2}{\partial t^2} \int_{l(t)} \frac{\left|\chi_{th}^{(3)}\right| I^2}{|r-r'|} dl(t) \tag{4.44}$$

where, $l(t)$ is the path, in 2-D geometry, where $|r-r'| = ct$; $N_1 = \frac{\Gamma}{4\pi v}$; $N_2 = \frac{1}{8\pi\varepsilon_0 (nc)^2 v}$ and γ_e is replaced by $\frac{\chi_{el}^{(3)} I}{n\varepsilon_0 c}$. According to Equation (4.25), we can rewrite Equation (4.44) for collected optoacoustic signals at two different light intensities as,

$$\Delta\tilde{p}_{tot} = N_2 \frac{\partial^2}{\partial t^2} \int_{l(t)} \frac{\left|\chi_{th}^{(3)}\right| \Delta I}{|r-r'|} dl(t) \tag{4.45}$$

where, ΔI is $I_2 - I_1$ and we suppose approximately light intensity to be a constant. By developing a model-based reconstruction algorithm for Equation (4.45), we can reconstruct images of $\chi_{th}^{(3)}$ of tissues. $\Delta\tilde{p}_{tot}$ can be obtained from two optoacoustic data measured at two different light intensities by using Equation (4.25). To develop a new model-based algorithm, we altered the algorithm described in [73] by rewriting Equation (4.45) as,

$$\Delta\tilde{p}_{tot} \approx \frac{H(t+\Delta t) - 2H(t) + H(t-\Delta t)}{(\Delta t)^2} \tag{4.46}$$

where, $H(t)$ is

$$H(t) = \int_{l(t)} \frac{\left|\chi_{th}^{(3)}\right| \Delta I}{|r - r'|} dl(t) \tag{4.47}$$

We analyzed the optoacoustic data obtained from a mouse, in-vivo, illuminated with two different light fluences, using a multispectral optoacoustic tomography scanner (MSOT256-TF; iThera Medical, Germany). Optoacoustic measurements were acquired at two light fluence $\varphi_{min} = 1.5$ and $\varphi_{max} = 9\ \mathrm{mJ/cm^2}$ and labeled $\hat{p}_{min} = \frac{p_{min}}{\varphi_{min}}$ and $\hat{p}_{max} = \frac{p_{max}}{\varphi_{max}}$, respectively. The maximum illumination employed herein is typically approved illumination for MSOT imaging, i.e. the measurements performed did not exceed the approved fluence limits for tissue imaging. Figure 4.4a and Figure 4.4b shows the reconstructed image of initial pressure rise at light fluence 1.5 and 9 mJ/cm2 (800 nm) respectively, after pre-processing the data acquired with a 200 kHz - 8 MHz band-pass filter (see Sec. 4.2). Images in Figure 4.4a and Figure 4.4b were reconstructed by the model-based algorithm introduced in [73] by considering p_{min} and p_{max} as purely thermal pressure. We next used the two acquired data set (p_{min} and p_{max}) and produced the images of $\chi_{th}^{(3)}$ contrast (Figure 4.4c) which is reconstructed by using the verified model-based algorithm based on Equations (4.46) and (4.47). Since light intensity is proportional to fluence, ΔI can be replaced by $\Delta\varphi = \varphi_{max} - \varphi_{mim}$ in Equation (4.47). Figure 4.4c was reconstructed using the verified model-based algorithm without pre-processing the data. The effect in Figure 4.4c is clearly understood as the high-frequency component of the data acquired and indicates that electro-optoacoustic pressure (nonlinearity) is more significant at a high-spatial frequency which is consistent with theoretical and experimental results presented in this chapter.

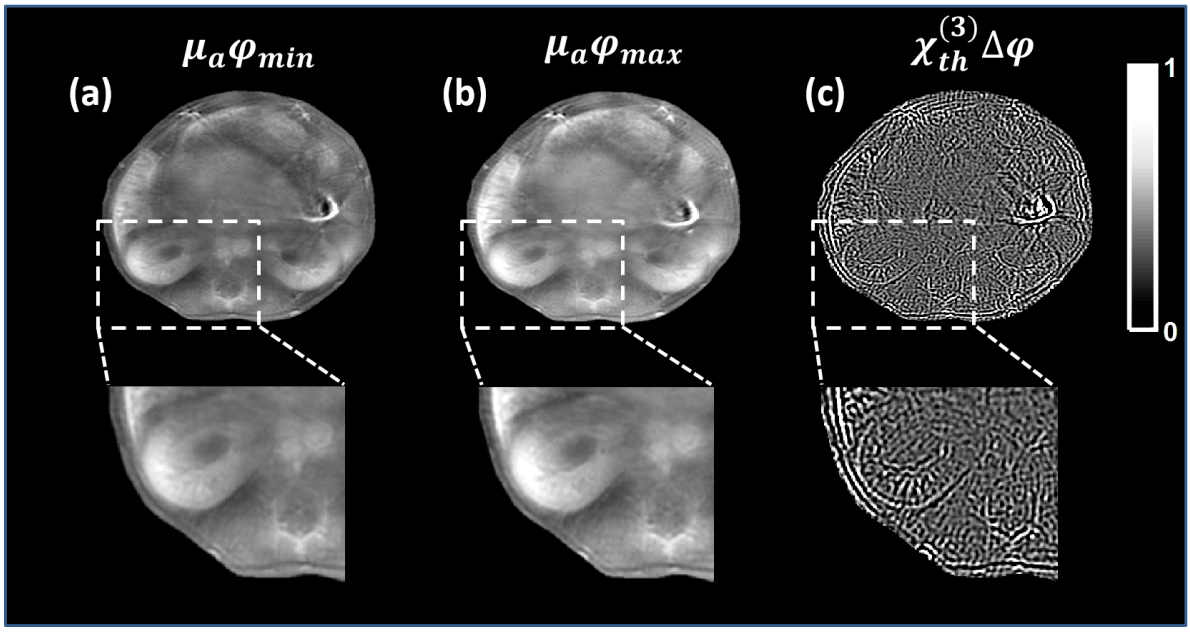

Figure 4.4. Optoacoustic imaging taken *in-vivo* through a mouse kidney cross-section. (a) and (b) Reconstructed image of absorption coefficient at light fluence 1.5 and 9 mJ/cm^2, respectively, 200 kHz - 8 MHz band-pass filter. (c) Reconstructed image of thermal nonlinear susceptibility ($\chi_{th}^{(3)}$) by using the electro-optoacoustic data, according to Equation (4.47).

4.5 Discussion

This study provides evidence that nonlinear variation of optoacoustic signal at fluences, used in biomedical optoacoustic imaging, may reflect primarily the effects thermally excited nonlinear susceptibility as the source of the electro-optoacoustic pressure. We demonstrate here that the electro-optoacoustic pressure appears to contribute significantly to the total pressure recorded and impart nonlinearity at high frequency components. In this case, using electro-optoacoustic pressure to reconstruct an image leads to a new contrast mechanism which represents the changes in the thermally excited nonlinear susceptibility of the sample.

These results have theoretical and practical implications in biomedical optoacoustic imaging, since optoacoustic imaging in preclinical and clinical settings is often

performed at relatively high fluences where the pressure response is likely to be nonlinear. Our approach of un-mixing and reconstructing the contribution of electro-optoacoustic pressure in the total measured pressure should be validated with more biological samples and extend this tool for obtaining more functional information and improving the quality of optoacoustic tomography and potentially many related optoacoustic imaging modalities, such as fluorescence molecular tomography and diffuse optical tomography.

Our results suggest that factors previously proposed to explain nonlinear response in optoacoustic micro- and mesoscopy, including nanobubbles [39, 40], changes in thermo-physical parameters [43, 66] or saturation of the absorption coefficient [42], are less likely to operate in nonlinear optoacoustic tomography. Our findings are consistent with the idea that higher light fluence in optoacoustic tomography does not cause sufficient local heating to trigger thermo-physical or phase changes, and they suggest that advances in optoacoustic imaging will require accurate modelling and correction of variations in optoacoustic signal at higher light fluence.

We validated and extended our mathematical considerations with experimental data obtained using phantoms. We initially focused on phantoms since they can be prepared with the desired dimensions, absorption and scattering properties. With biological samples, in contrast, the distribution of absorption coefficients cannot be accurately known a priori. In addition, accurate reconstruction requires accurate modelling of the speed of sound through the sample and medium, which is easily estimated in phantoms by comparing the original dimensions with those in the reconstructed image. Our results with phantoms demonstrate that the electro-optoacoustic pressure can alter the measured optoacoustic signal and be the main contributor to optoacoustic nonlinearity.

Our results further suggest that the electro-optoacoustic pressure can be extracted from the total pressure. The aim of electro-optoacoustic reconstruction is to generate an image from electro-optoacoustic pressure data, since electro-optoacoustic pressure is proportional to the variation of nonlinear susceptibility (Equation (4.24)) and so reconstructed images provide biologically useful results about the changes in the nonlinear susceptibility of light absorbers in the sample. Usually the total measured optoacoustic signal is considered to be equivalent to thermal pressure because the electro-optoacoustic pressure is not considered. However, our results show that at fluences used for biological imaging, electro-optoacoustic pressure might make a substantial contribution to the total pressure and therefore must be extracted from the total pressure in order to generate the image of the nonlinear susceptibility as a new contrast mechanism.

5 Nonlinear artifact correction in optoacoustic imaging

5.1 Introduction

In chapter 2, we described the optoacoustic signal behaves nonlinearly at light fluences above approximately 6 mJ/cm^2, which may affect the interpretation and quantification of optoacoustic measurements. Using appropriately constructed physical phantoms, we provided evidence that at laser fluences above a threshold, electro-optoacoustic pressure nonlinearly alters the detected optoacoustic pressure. In this chapter we will study how nonlinearity effects the reconstructed optoacoustic images and develop an algorithm that corrects for the effects of nonlinearity in the reconstructed images. We demonstrate that the correction algorithm can accurately reverse nonlinear effects in the image, and improve the quantitative accuracy of optoacoustic imaging.

The presence of nonlinear effects reduces the quantitative accuracy of optoacoustic measurements employed in spectroscopic or imaging applications, since current optoacoustic systems do not take this nonlinearity into account. Instead, they assume that the optoacoustic signal is linearly proportional to the fluence of the illuminating laser [20]. For example, inversion algorithms employed in optoacoustic tomography assume that signals vary linearly with light fluence and the concentration of chromophores illuminated by the laser. This information is then employed to visualize pathophysiological information [16]. Nonlinear behavior of the optoacoustic signal at higher light fluences means that conventional reconstruction algorithms may offer erroneous estimates of chromophore concentrations and readings of tissue pathophysiology.

Based on these results, we developed an algorithm that corrects for the effects of nonlinearity and that substantially improves optoacoustic tomographic images. Further optimization of the proposed algorithm and validation in biological samples may provide a highly useful tool for improving the quality of reconstructed images in optoacoustic tomography. Our results may also have important implications for nonlinear behavior in optoacoustic micro- and mesoscopy.

5.2 Methods

5.2.1 Phantoms

Tissue-mimicking homogeneous phantoms (analyzed in Figure 5.4 and Figure 5.5) were prepared as described in section 4.2.1. A tissue-mimicking heterogeneous phantom (shown in Figure 5.1) was prepared to test the effects of the correction algorithm on reconstruction quality. The agar cube (1 x 1 x 1 cm) contained three smaller agar tubes to mimic tissue heterogeneity, black India ink for optical absorption,

and intralipid for optical scattering. The phantom was prepared as cubes (1 x 1 x 1 cm) by mixing agar (2% solution in deionized water, 05039-500G, Sigma-Aldrich, Steinheim, Germany) with black India ink (Higgins, Texas) and intralipid (20% emulsion, I141-100ML, Sigma). The ink was first diluted using deionized water as needed in order to obtain the desired final absorption coefficients, as determined using a spectrometer (LS-1-cal, USB4000; Ocean Optics, Germany). The amount of Intralipid was also varied in order to achieve different reduced scattering coefficients [51]. First, the ink and intralipid were mixed, then the 2% agar was added, and the entire mixture was heated in a microwave oven.

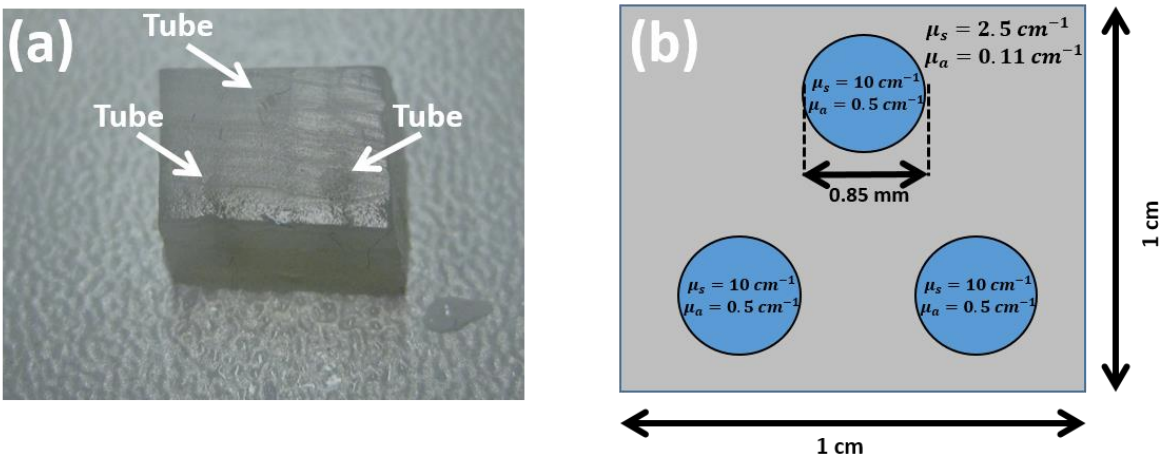

Figure 5.1 Schematic of the heterogeneous agar phantom. (a) The agar cube ($1 \times 1 \times 1$ cm) was impregnated with ink and Intralipid, and it contained three embedded agar tubes. (b) Dimensions and parameters of the phantom.

5.2.2 Optoacoustic data acquisitions

We used the single transducer setup shown in Figure 3.1a to acquired data from homogeneous phantoms, as shown in Figure 5.4-Figure 5.5.

To examine the effects of the nonlinearity from the measured optoacoustic pressure on reconstruction of the heterogeneous phantom, a small-animal multispectral optoacoustic tomography scanner (MSOT256-TF; iThera Medical, Germany) and

imaging setup shown in Figure 5.2 were used. This imaging system has been described in detail elsewhere [59]. A tunable OPO laser (InnoLas Laser) illuminated a water-filled field of view with a diameter of 4.05 cm. The phantom was illuminated on only one side by guiding the light with a four-branch fiber bundle (WF 179, numerical aperture 0.22, tip diameter 2.5 mm; CeramOptec GmbH, Bonn, Germany). The phantom was illuminated with only one of the branches and the other three branches were blocked. Fluences of 4 and 16 $\mathrm{mJ/cm^2}$ were used to induce, respectively, linear and nonlinear optoacoustic signals. These signals were detected using a 256-element ultrasound transducer array with a central frequency of 5 MHz and a detector bandwidth of 90%. Signals were amplified and recorded using a data acquisition card [59].

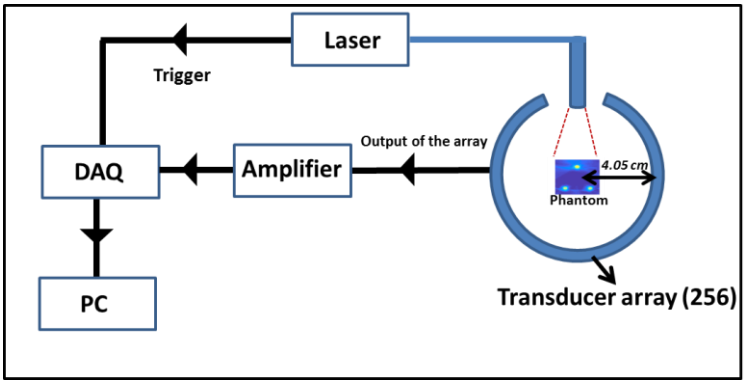

Figure 5.2 Schematic of the set-ups used to remove nonlinear optoacoustic effects from the heterogeneous agar phantom. The set-up used to collect optoacoustic signal from a heterogeneous phantom containing three embedded agar tubes.

5.2.3 Development of an algorithm to correct for the nonlinearity

Optoacoustic data collected from the heterogeneous phantom in Figure 5.1 using the set-up shown in Figure 5.2 were reconstructed into images based on initial pressure rise using a model-based reconstruction algorithm that solves the acoustic wave equation [20]. For each measurement, the fluence distribution was used to correct for light fluence as follows. The light fluence distribution inside the sample (Figure 5.3)

was calculated by solving the diffusion equation [Equation (5.1)] using the finite volume method and Robin boundary conditions [74],

$$\mu_a \varphi - \nabla . [D . \nabla \varphi] = q \tag{5.1}$$

where φ is the light fluence, D indicates the spatially dependent diffusion coefficient of the medium ($D = \frac{1}{3(\mu_a + \mu_s')}$), μ_s' is the reduced scattering coefficient, μ_a represents the optical absorption coefficient, and q is the source term. Then, light fluence correction was performed after reconstruction to remove effects of fluence variation on the initial pressure rise. The initial pressure rise p in the sample as a result of laser illumination is given by,

$$p = \Gamma \mu_a \varphi \tag{5.2}$$

The initial pressure rise was divided by the estimated light fluence to obtain an approximate absorption coefficient distribution. Equation (5.2) shows the linear relationship of the initial pressure rise, depending on optical absorption coefficient, and light fluence.

The approximate absorption coefficient will have an accurate distribution in the linear regime but not in the nonlinear regime, necessitating the use of Equation (5.2) to remove the effects of nonlinearity from the total optoacoustic pressure. Hence, a correction algorithm was applied before reconstructing data. The correction algorithm is based on the idea that nonlinearity in the dielectric constant (Equations (4.23) and (4.24)) is the main cause of optoacoustic nonlinearity, which can be corrected by

removing the electro-optoacoustic pressure from the total optoacoustic pressure. Therefore, Equation (4.14) can be rewritten as

$$p_{tot} = m' \hat{p}_{th} + n' \hat{p}_{eo}, \tag{5.3}$$

where m' and n' are two constants, $\hat{\mathrm{p}}_{\mathrm{th}} = \mathrm{p}_{\mathrm{th}}/|\mathrm{p}_{\mathrm{th}}|$ is the normalization of the thermal pressure and $\hat{p}_{\mathrm{e}} = \mathrm{p}_{\mathrm{e}}/|\mathrm{p}_{\mathrm{e}}|$ is the normalization of the electro-optoacoustic pressure. Since at low fluence, the electro-optoacoustic pressure is small compare to P_{th} (Equation (4.24)), the contribution of electro-optoacoustic pressure in the measured optoacoustic signal at low fluences (p_{min}) can be neglected (section 4.4.2). As a result, n' in Equation (5.3) is taken to be negligible when fluence is sufficiently low, leading to

$$\hat{p}_{th} = \frac{p_{min}}{|p_{min}|} \tag{5.4}$$

By using Equations (4.40) and (4.41), we find that,

$$\hat{p}_{eo} = \frac{\hat{p}_{max} - \hat{p}_{min}}{|\hat{p}_{max} - \hat{p}_{min}|} \tag{5.5}$$

where p_{min} and p_{max} are the total pressure at very low and high fluence, respectively. The coefficients m' and n' can be extracted from the measured data for each fluence by minimizing the mean square difference between the measured total pressure (p) and the theoretical pressure:

$$min\|p - M\tilde{p}\|^2 \tag{5.6}$$

where $\|.\|$ is an l_2 norm, $\mathrm{M} = [\mathrm{m}'\ \mathrm{n}']$, and $\tilde{\mathrm{p}} = \begin{bmatrix} \hat{\mathrm{p}}_{\mathrm{t}} \\ \hat{\mathrm{p}}_{\mathrm{e}} \end{bmatrix}$. The solution of Equation (5.6) was calculated by the least-squares QR algorithm [75]. Therefore, using Equations (5.4),

(5.5), and (5.6), the thermal pressure was extracted from the total optoacoustic pressure for each single transducer. This requires determining the normalized total pressure at low fluence ($\hat{p}_{min}$) and high fluence ($\hat{p}_{max}$), so optoacoustic data were acquired at low fluence and high fluence by scanning the homogeneous phantom using setup shown in Figure 3.1a and the heterogeneous phantom shown in Figure 5.1 using the setup shown in Figure 5.2. In the end, the thermal pressure was extracted. In the heterogeneous phantom, the reconstructed data were divided by the fluence distribution in Figure 5.3 to remove fluence effects based on Equation (5.2), allowing determination of the absorption coefficient.

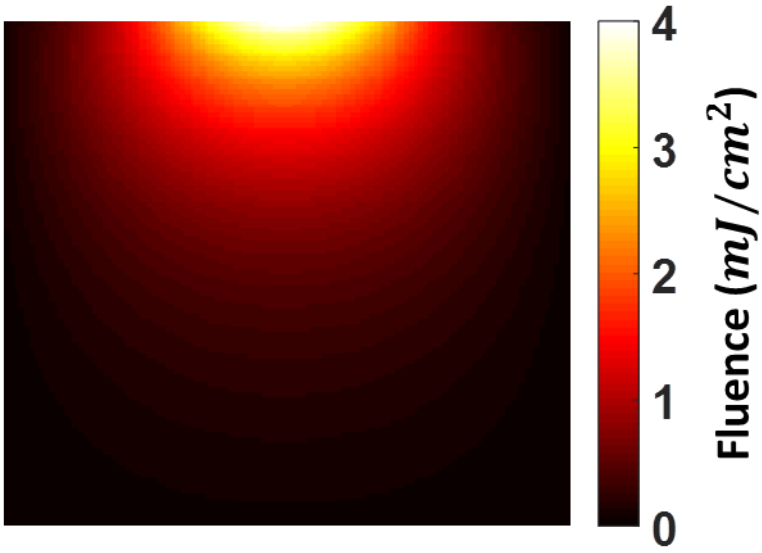

Figure 5.3 Distribution of light fluence inside the phantom by solving the diffusion equation.

5.3 Results

In this section, we experimentally verified the algorithm that corrects for the effects of the nonlinearity. In section 5.3.1, the algorithm is examined for the optoacoustic pressure collected from three homogeneous phantoms using the setup shown in

Figure 3.1a. Then, we tested the algorithm on a heterogeneous phantom by correcting the optoacoustic signals measured with the setup shown in Figure 5.2 and then testing whether that leads to more accurate thermal pressures and therefore higher-quality reconstructions.

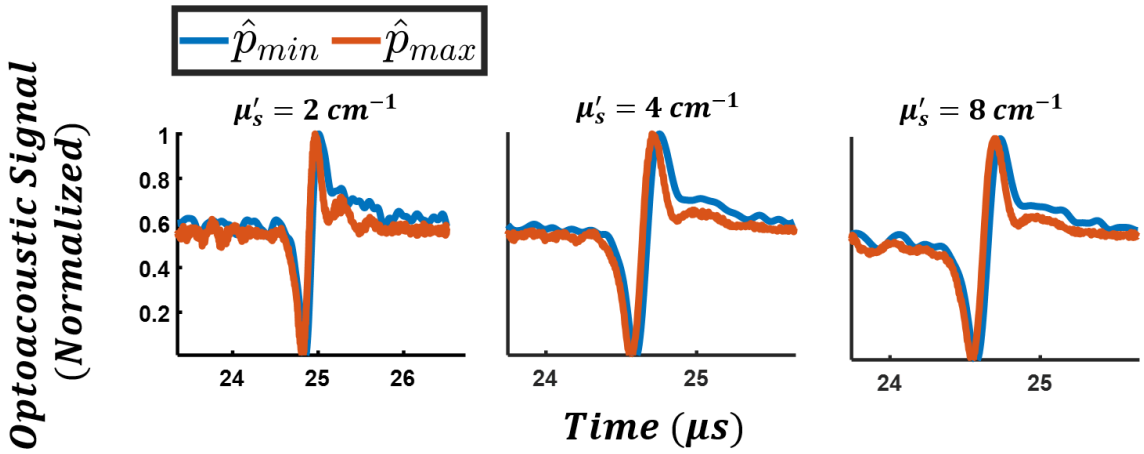

Figure 5.4. Tissue-mimicking phantoms containing ink, agar, and intralipid with an absorption coefficient $\mu_a' = 0.1\ \mathrm{cm}^{-1}$ were analyzed. The phantoms were formulated with different amounts of intralipid to give reduced scattering coefficients of $\mu_s' = 2, 4, \text{or } 8\ \mathrm{cm}^{-1}$. Normalized optoacoustic pressure after illumination at 3 $\mathrm{mJ/cm^2}$ ($\hat{p}_{min}$) or 20 $\mathrm{mJ/cm^2}$ ($\hat{p}_{max}$) at 800 nm.

5.3.1 Single transducer measurement

To validate the developed algorithm (section 5.2.3), we measured the optoacoustic signal from three tissue-mimicking agar cubes having different reduced scattering coefficients, which allowed us to vary the extent of nonlinearity (Chapter 2). The phantoms consisted of ink and intralipid such that for a laser operating at a wavelength of 800 nm, the absorption coefficient was uniform ($\mu_a = 0.1\ \mathrm{cm}^{-1}$) and the reduced scattering coefficient was also uniform but different for each phantom ($\mu_s' = 2, 4, \text{or } 8\ \mathrm{cm}^{-1}$). Figure 5.4 depicts the normalized optoacoustic signals at a light fluence of 3 $\mathrm{mJ/cm^2}$ ($\hat{p}_{min}$), which is low enough to trigger a linear response; or a fluence of 20

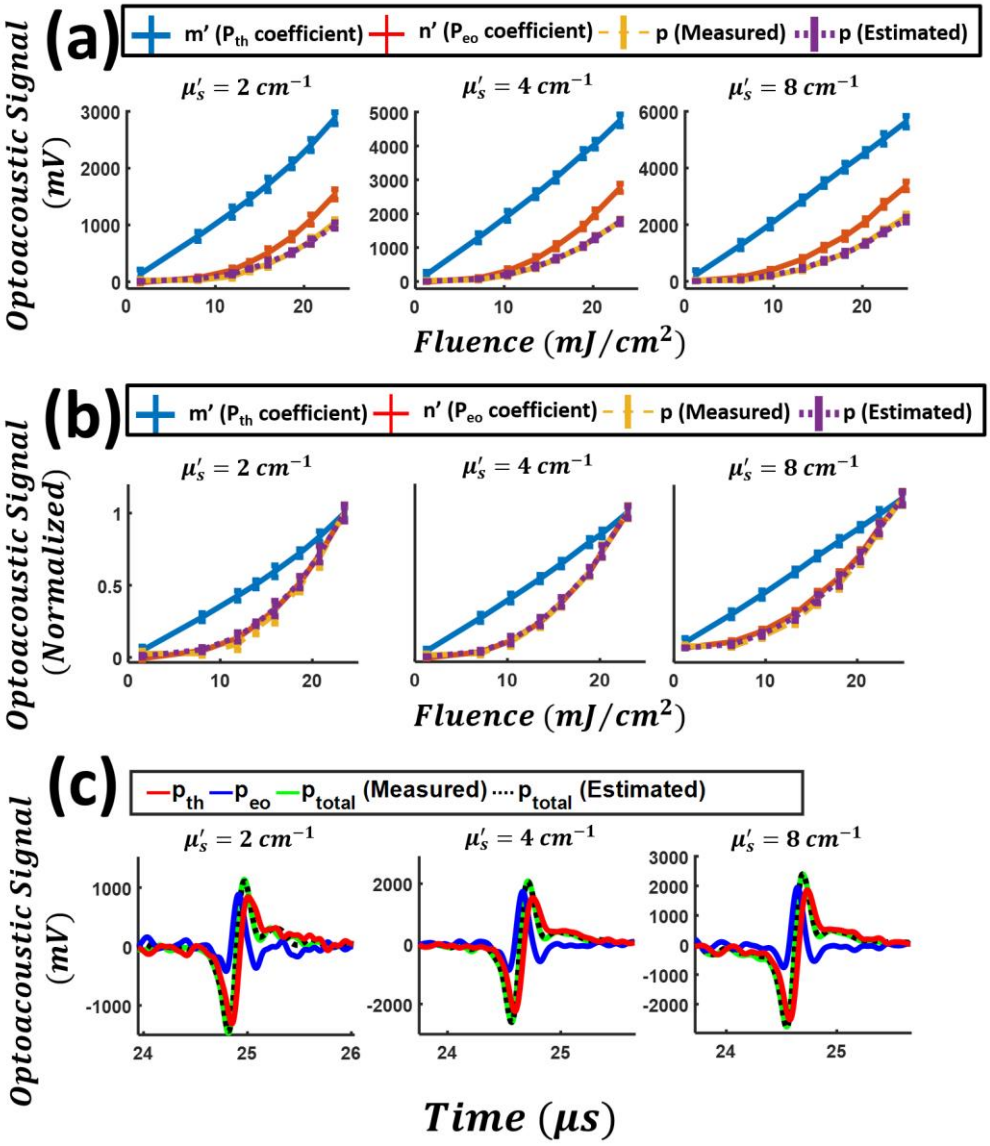

Figure 5.5. Description of total optoacoustic pressure as a linear combination of electro-optoacoustic and thermal pressures, and demonstration of nonlinear electro-optoacoustic pressure at high fluences. Tissue-mimicking phantoms containing ink, agar, and intralipid with an absorption coefficient $\mu_a' = 0.1\ \mathrm{cm}^{-1}$ were analyzed. The phantoms were made with different amounts of intralipid to give reduced scattering coefficients of $\mu_s' = 2, 4, \text{or } 8\ \mathrm{cm}^{-1}$. (a) Measured and estimated total pressure at the zero crossing of $\hat{p}_{min}$ in the three phantoms. The m' and n' curves show changes in thermal and electro-optoacosutic pressures respectively, as a function of fluence. (b) Normalization of the curves in panel (a) to the maximum value. (c) Measured and estimated total pressure at a fluence of 22.5 mJ/cm^2, together with the electro-optoacoustic component p_{eo} and thermal component p_{th}.

$\mathrm{mJ/cm^2}$ ($\hat{\mathrm{p}}_{\max}$), which is enough to stimulate a nonlinear response. The two signals $\hat{\mathrm{p}}_{\min}$ and $\hat{\mathrm{p}}_{\max}$ approximately showed similar shapes but were shifted slightly in time.

To examine the algorithm, we measured total optoacoustic pressure p for different light fluences. For three phantoms, we obtained $\hat{\mathrm{p}}_{th}$, as defined in Equation (5.4), and $\hat{p}_{eo}$, as defined in Equation (5.5). The electro-optoacoustic pressure coefficients (n') and thermal pressure coefficient (m') can be extracted from the measured data for each fluence by Equation (5.6) and compared with experimental measurements at the time point when $\hat{\mathrm{p}}_{\min}$ passed through zero. At all three scattering levels, the electro-optoacoustic pressure coefficient (n') showed a nonlinear dependence with fluence, whereas the thermal pressure coefficient (m') showed a linear dependence (Figure 5.5a), which is consistent with Equation (4.24). Normalization of the data revealed nearly perfect overlap between the electro-optoacoustic pressure and total pressure (Figure 5.5b), suggesting that at high fluence, nonlinearity in electro-optoacoustic pressure may explain most, if not all, nonlinearity in the overall optoacoustic signal. The validity of these results and the algorithm is reflected in the perfect overlap of measured and estimated optoacoustic signals as a function of fluence (purple and yellow curves, Figure 5.5a-b). This overlap extended over the entire signal: Figure 5.5c, for instance, shows the excellent fit between measured and estimated optoacoustic signals at a fluence of 22.5 $\mathrm{mJ/cm^2}$.

5.3.2 Optoacoustic tomography

We then tested the developed algorithm (Sec. 5.2.3) by correcting the measured optoacoustic signals for each single transducer of an array and then testing whether that leads to more accurate thermal pressures and therefore higher-quality reconstructions. Two measurements were performed on a heterogeneous phantom consisting of an agar cube containing three smaller agar tubes as additives to affect

absorption. To show the effects of the nonlinearity and the correction algorithm, the first experiment was performed at low fluence (linear area) and the second experiment was carried out at high fluence (nonlinear area).

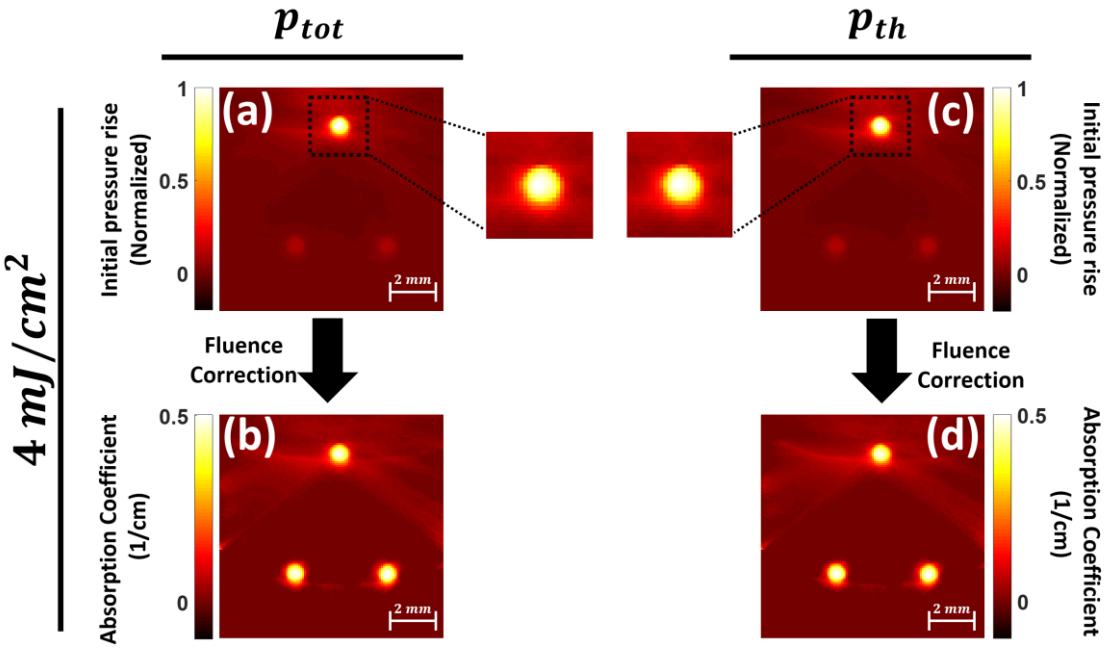

Figure 5.6 Correction for fluence and the nonlinearity to improve optoacoustic image reconstruction. An agar cube containing three smaller agar tubes was illuminated at a fluence of 4 mJ/cm2, where the optoacoustic signal behaves linearly. The illumination source is near the top of all images. The first row shows the distribution of the initial pressure rise based on reconstruction of total pressure (p_{tot}) or thermal pressure (p_{th}). Zoomed-in images of the upper agar tube are also shown in the middle. The second row shows the distribution of absorption coefficients obtained by correcting the data in the first row for depth-dependent changes in fluence.

We first illuminated the phantom at a fluence of 4 mJ/cm^2, where the optoacoustic signal varies linearly with fluence. Figure 5.6a depicts the distribution of the initial pressure rise after reconstructing the measured total pressure (p). The pressure rise was greater in the upper part of the sample (closer to the illumination source) than in

the lower part, consistent with what occurs in diffusive tissue. As a result, the two lower agar tubes appeared much fainter than the upper one, even though all three tubes had the same absorption coefficient and so should appear identical. Figure 5.6b shows that by correcting for depth-dependent changes in fluence, the reconstructed image correctly depicted all three tubes as similar. Figure 5.6c shows the initial pressure rise obtained by reconstructing only the thermal pressure ($\mathrm{p_{th}}$) extracted from the measured total pressure ($\mathrm{p_{tot}}$). Figure 5.6d is the absorption coefficient map obtained from the data in Figure 5.6c by correcting for fluence. The similarities between Figure 5.6b and Figure 5.6d and between the zoomed-in regions in Figure 5.6a and Figure 5.6c indicate that at low light fluence, we were able to reconstruct equally accurate optoacoustic images using either total pressure or thermal pressure. This means that nonlinearity did not contribute significantly to total pressure.

We obtained substantially different results when we illuminated the same phantom at a fluence of 16 $\mathrm{mJ/cm^2}$, where the optoacoustic signal varies nonlinearly with fluence. Figure 5.7a shows the distribution of the initial pressure rise based on reconstruction of total pressure ($\mathrm{p_{tot}}$); as at the lower fluence (Figure 5.6a), the two lower tubes appeared much fainter than the upper tube. Figure 5.7b shows the distribution of absorption coefficients after correcting for depth-dependent changes in fluence. While at lower fluence this correction was sufficient to restore the equivalence of all three tubes (Figure 5.6b), it was insufficient at higher fluence. Figure 5.7c shows the distribution of initial pressure rise based on reconstruction with only thermal pressure (p_{th}). The image is similar to that obtained based on reconstruction with total pressure (Figure 5.7a) but with improvements, such as the absence of a zone of negative pressure rise above the upper tube observed after reconstruction based on total pressure (zoomed-in regions in Figure 5.7a and Figure 5.7c). This indicates that at

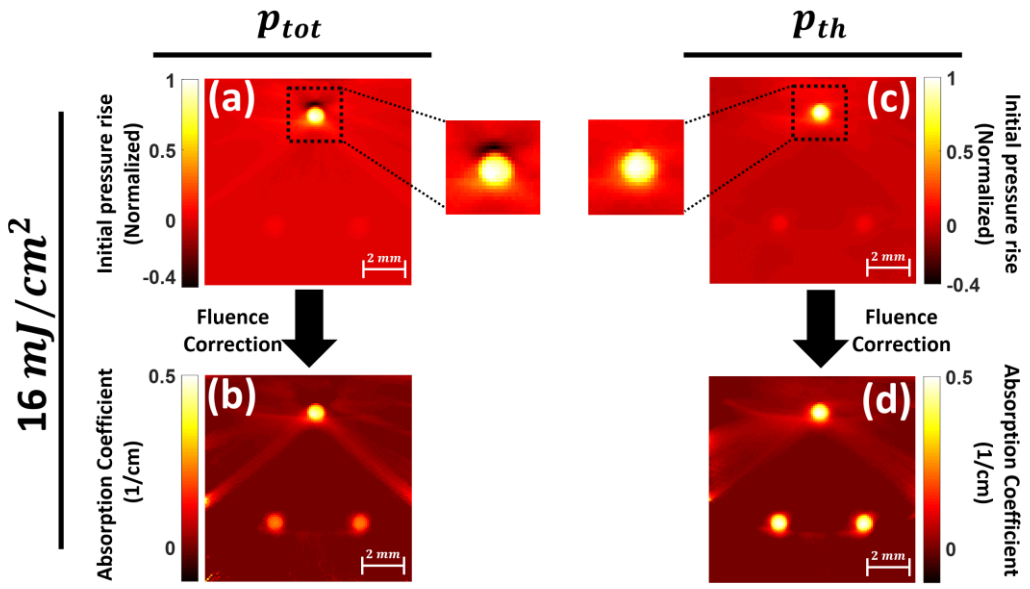

Figure 5.7 Correction for fluence and nonlinearity to improve optoacoustic image reconstruction at high fluence. An agar cube containing three smaller agar tubes was illuminated at a fluence of 16 mJ/cm^2, where the signal behaves nonlinearly. The illumination source is near the top of all images. The first row shows the distribution of the initial pressure rise based on reconstruction of total pressure (p_{tot}) or thermal pressure (p_{th}). Zoomed-in images of the upper agar tube are also shown in the middle. The second row shows the distribution of absorption coefficients obtained by correcting the data in the first row for depth-dependent changes in fluence.

higher fluence, image reconstruction based on total pressure was less accurate than reconstruction based on thermal pressure, reflecting the non-negligible nonlinear variations. These results were confirmed by comparing absorption coefficient maps (Figure 5.7b and Figure 5.7d): all three tubes appeared correctly with the same absorption coefficient only in the map based on thermal pressure. These results support the idea that nonlinearity at higher fluence can distort reconstructed absorption coefficients, substantially reducing the image quality. Our results suggest that at fluences where the optoacoustic signal behaves nonlinearly, the nonlinear variations

should be isolated and removed before image reconstruction in order to maximize final image quality.

5.4 Discussion and conclusion

We demonstrate here that at fluences lower than a certain threshold, which in our phantoms was $6\,\mathrm{mJ/cm^2}$, the electro-optoacoustic pressure does not contribute significantly to total pressure, such that using total pressure in reconstruction leads to the same high-quality images as using thermal pressure on its own. At fluences higher than the threshold, however, electro-optoacoustic pressure can contribute significantly to total pressure, and the nonlinearity of electro-optoacoustic pressure may cause the total pressure to behave nonlinearly. In this case, using the total pressure to reconstruct images leads to inaccuracy. Only by removing the specific contribution of electro-optoacoustic pressure can images be reconstructed accurately. Our results have potentially profound theoretical and practical implications for optoacoustic imaging, since optoacoustic imaging in preclinical and clinical settings is often performed at relatively high fluences where the pressure response is likely to be nonlinear. Our approach of isolating the specific contribution of thermal pressure in order to exclude the contribution of electro-optoacoustic pressure should be validated on biological samples and developed as a tool for improving the quality of optoacoustic tomography and potentially many related optoacoustic imaging modalities, such as fluorescence molecular tomography and diffuse optical tomography.

In this study, we focused on phantoms since they can be prepared with the desired dimensions, absorption and scattering properties. With biological samples, in contrast, the distribution of absorption coefficients cannot be accurately known a priori. In addition, accurate reconstruction requires accurate modelling of the speed of sound

through the sample and medium, which is easily possible in phantoms by comparing the original dimensions with those in the reconstructed image.

Our results suggest that while fluence correction alone may be adequate for optoacoustic reconstruction at lower fluence (linear regime), correction should also be made for nonlinearity at higher fluence (nonlinear regime). If not, reconstruction may give unreliable images that cannot be accurately quantified, undermining the ability of optoacoustic tomography to determine, for example, the distribution of hemoglobin, lipids or other biological or functional absorbers in tissues [16]. The aim of optoacoustic reconstruction is to generate an image from thermal pressure data, since thermal pressure is proportional to the absorption coefficient [Equation (5.2)] and so reconstructed images provide biologically useful results about the concentrations of light absorbers in the sample. Usually the total measured optoacoustic signal is considered to be equivalent to thermal pressure because the electro-optoacoustic pressure is considered to be negligible. However, our results show that at fluences above the threshold, around 6 mJ/cm2 in this study and our previous study [65], electro-optoacoustic pressure might make a substantial contribution to total pressure and therefore must be subtracted from that pressure in order to generate accurate values of thermal pressure for high-quality image reconstruction.

We demonstrated that subtracting non-negligible nonlinear variations from the measured optoacoustic pressure indeed improved reconstructions of a heterogeneous phantom containing three equivalent agarose tubes containing ink at different depths. After reconstruction based on total pressure, the three tubes were not associated with the same absorption coefficients after fluence correction, even though the coefficients were identical (Figure 5.7b). In addition, the reconstruction showed an implausible region of negative pressure rise above the upper tube (Figure 5.7a), which cannot give

rise to physically meaningful absorption coefficients. When we corrected for both fluence distribution as well as nonlinear electro-optoacoustic pressure, we were able to obtain a distribution of positive absorption coefficients in which all three tubes appeared identical (Figure 5.7d).

This study demonstrates that failure to correct for such nonlinearity can substantially reduce the quality of tomographic reconstructions of heterogeneous tissue-mimicking phantoms. Hence, electro-optoacoustic pressure, not traditionally considered in optoacoustics data analysis, may substantially affect the total pressure and should be considered at fluences above a certain threshold. A correction algorithm is proposed to correct for these nonlinear variations. Future work should validate the algorithm in biological samples as well as explore optoacoustic nonlinearity in greater detail, including the factors affecting the threshold fluence above which nonlinear behavior appears. The correction algorithm proposed here may become an essential tool for ensuring accurate optoacoustic tomography when laser fluence lies outside the linear response range of the sample.

6 Conclusion and Future Outlook

This thesis demonstrates that nonlinear effects can be observed in optoacoustic mesoscopy and tomography at light fluences which are within ANSI safety limits and typically used in optoacoustic imaging. Our results suggest that conventional reconstruction algorithms for optoacoustic imaging, which assume a linear behavior of an optoacoustic signal as a function of light fluence, may be less accurate at light fluences above a certain threshold. In our measurements, this threshold was found to be ~ 6 mJ/cm^2 which relies on measurement under the maximum permissible exposure limits [53]. Therefore, it was necessary to further investigate a proper correction for the nonlinear response to improve tomographic or spectral unmixing quantification when using pulses of higher energy. As far as we are aware, this is the first time that the nonlinearity in both mesoscopic and macroscopic regimes was reported. Consequently, we found it is essential to characterize the observed nonlinearity and perform

systematic studies to examine additional factors that may contribute to nonlinear optoacoustics.

To this end, the nonlinearity was investigated as a function of the optical absorption coefficient, reduced scattering coefficient, and in relation to the material and wavelength employed. As far as we are aware, this is the first observation that the optoacoustic signal and the nonlinearity are a function of the scattering coefficient. The amplitude of the optoacoustic signal for the non-scattering material was linear and an order of magnitude lower than that of the scattering material. This observation may relate to the light propagation pattern inside the phantom. Photons inside the non-scattering phantom propagate along diverging straight lines, resulting in the effective absorption cross-section and excitation energy deposited on the absorber to be less than in the case of the diffusive light propagation, which allows multiple photon absorption by absorbers. Our results suggest that it is necessary to further theoretically and experimentally investigate the effect of the scattering coefficient on the optoacoustic signal in mesoscopic regimes in the future. In addition, it was observed that the nonlinearity might be affected by the molecular nature of absorbers and the energy of photons.

We interrogated the optoacoustic nonlinearity in the macroscopic regime by using a transmission mode setup. We were not able to explain the measured nonlinearity using variations of light fluences at different depth. Therefore, we suspected that the local temperature rise is not the main cause of the observed nonlinearity, since the generated temperature is directly proportional to light fluence. Next, this thesis theoretically and experimentally explored the influence of temperature on the optoacoustic pressure. The optoacoustic pressure was derived by expressing the Grueneisen parameter as a function of temperature. The nonlinear term in the derived

equations had a singularity at the temperature where the thermal expansion coefficient becomes zero. Our theoretical results suggested that the optoacoustic pressure is linearly dependent on temperature except in cases where the conditions for singularity are satisfied. Our experimental results confirmed that the peak-to-peak value of the optoacoustic signal as a function of fluence becomes more nonlinear with temperature of the probed medium getting close to 4^{o}C. Hence, we conclude that the observed nonlinearity in our measurements at room temperature cannot be explained by the local temperature rise induced by the laser. Furthermore, we observed that frozen water (ice) generated a stronger optoacoustic signal than liquid water. In addition, the optoacoustic spectrum of ice was completely different from that of water. We believe that a more detailed analysis on the mentioned singularity and the unusual optoacoustic properties of ice can be performed.

We subsequently developed a theoretical framework to explain the observed nonlinearity at room temperature in terms of the behavior of an absorbing dielectric slab placed in an electric field. Our results suggested that the recorded optoacoustic signal at the transducer has an additional contribution, along with the signals generated by the optical absorption coefficient (thermal pressure). The additional pressure signal is due to the effects of thermally excited nonlinear susceptibility of the electro-optoacoustic pressure. Therefore, electro-optoacoustic pressure was identified as a primary contributor to optoacoustic nonlinearity at fluences used in biological imaging. We demonstrated that reconstructing the electro-optoacoustic pressure provides images with a new contrast mechanism related to the thermally excited nonlinear susceptibility. While the electro-optoacoustic pressure has not been traditionally considered in optoacoustics data analysis, it may substantially affect the total pressure

and should be considered at high-spatial frequency. We have furthermore developed a reconstruction algorithm to recover the electro-optoacoustic pressure maps.

Moreover, we believe that the probed medium can generate an electro-optoacoustic pressure stronger than what is shown in this work. The thermal response time associated with the change in the susceptibility of the medium is often quite long (microseconds or milliseconds) [67]. Therefore, the nanosecond time scale (the laser pulse duration) is too short for a sufficient development of such effects (nonlinear susceptibility). As a future study, we can develop a new experimental setup by using two lasers to optimize the efficiency of the electro-optoacoustic stimulation. In this setup, the first laser will be used to thermally excite the nonlinear susceptibility in the medium and then the second laser will generate a light pulse after a certain time delay, in the order of the thermal response time, to capture the electro-optoacoustic pressure. By optimizing the time delay (thermal response time), the maximum value of the electro-optoacoustic pressure can be acquired.

We demonstrated that the electro-optoacoustic pressure can significantly contribute to the total pressure at relatively high fluences where the optoacoustic signal behaves nonlinearly. Therefore, using the total pressure to reconstruct optoacoustic images may be unreliable. In this work we have hence developed an algorithm to remove the contribution of electro-optoacoustic pressure to generate images that are more representative of optical absorption coefficient distribution. By using tissue-mimicking phantoms with the desired dimensions, optical absorption and optical scattering properties, we validated the correction algorithm that was able to accurately separate the thermal and electro-optoacoustic pressure distributions. The algorithm can substantially increase the quality of tomographic reconstructions by removing nonlinear effects. Future work should validate the algorithm in biological samples. The

correction algorithm proposed here may become an essential tool for ensuring accurate optoacoustic tomography, since optoacoustic imaging in preclinical and clinical settings is often performed at relatively high fluences where the pressure response is likely to be nonlinear.

List of Publications

- **J. Malekzadeh-Najafabadi**, J. Prakash, V. Ntziachristos, “Nonlinear optoacoustic readings from diffusive media at near-infrared wavelengths”, Journal of biophotonics, 2018.

- **J. Malekzadeh-Najafabadi**, J. Prakash, J. Ripoll, V. Ntziachristos, “Contribution of nonlinear changes in optoacoustic tomography”, Nature. Communications. 2021. (Submitted)

- **J. Malekzadeh-Najafabadi**, J. Prakash, V. Ntziachristos, “Temperature effects on optoacoustic nonlinearity”, 2020. (In Process)

- **J. Malekzadeh-Najafabadi**, J. Prakash, V. Ntziachristos, “Nonlinear artifact correction in optoacoustic imaging”, 2020. (In Process)

- V. Gujrati, J. Prakash, **J. Malekzadeh-Najafabadi**, A. Stiel, U. Klemm, G. Mettenleiter, M. Aichler, A. Walch, V. Ntziachristos, “Bioengineered bacterial vesicles as biological nano-heaters for optoacoustic imaging”, Nature communications, 2019.

- J. Prakash, M. Seyedebrahimi, A. Ghazaryan, **J. Malekzadeh-Najafabadi**, V. Gujrati, V. Ntziachristos, “Short-wavelength optoacoustic spectroscopy based on water muting” Proceedings of the National Academy of Sciences, 2020.

- A. Longo, S. Morscher, **J. Malekzadeh-Najafababdi**, D. Jüstel, C. Zakian, V. Ntziachristos, “Assessment of hessian-based Frangi vesselness filter in optoacoustic imaging”, Photoacoustics, 2020.

- S. Ovsepian, Y. Jiang, T. Sardella, **J. Malekzadeh-Najafabadi**, N. Burton, X. Yu, V. Ntziachristos, “Visualizing cortical response to optogenetic stimulation and sensory inputs using multispectral handheld optoacoustic imaging”, Photoacoustics, 2020.

- I. Olefir, A. Ghazaryan, H. Yang, **J. Malekzadeh-Najafabadi**, S. Glasl, P. Symvoulidis, V. O’Leary, G. Sergiadis, V. Ntziachristos, S. Ovsepian, “Spatial

and spectral mapping and decomposition of neural dynamics and organization of the mouse brain with multispectral optoacoustic tomography", Cell reports, 2019.

- V. Neuschmelting, K. Kim, **J. Malekzadeh-Najafabadi**, S. Jebiwott, J. Prakash, A. Scherz, J. Coleman, M. Kircher, V. Ntziachristos, "WST11 vascular targeted photodynamic therapy effect monitoring by multispectral optoacoustic tomography (MSOT) in mice", Theranostics , 2018.

- N. Liu, V. Gujrati, **J. Malekzadeh-Najafabadi**, J. Fuenzalida Werner, U. Klemm, L. Tang, Z. Chen, Y. Huang, J. Prakash, A. Stiel, G. Mettenleiter, M. Aicheler, A. Blutke, A. Walch, K. Kleigrewe, D. Razansky, M. Sattler, V. Ntziachristos, "Croconaine-based nanoparticles enable efficient optoacoustic imaging of murine brain tumors", Photoacoustics, 2021.

- H. Mohr, S. Ballke, N. Bechmann, S. Gulde, **J. Malekzadeh-Najafabadi**, V. Ntziachristos, K. Steiger, T. Wiedemann, N. S. Pellegata, "Mutation of the Cell Cycle Regulator p27kip1 Drives Pseudohypoxic Pheochromocytoma Development", Cancers, 2021.

List of Figures

($ptot$) or thermal pressure (pth). Zoomed-in images of the upper agar tube are also shown in the middle. The second row of image shows the distribution of absorption coefficients obtained by correcting the data in the first row for depth-dependent changes in fluence..... 78

List of Tables

Bibliography

1. Beckmann, E.C., *CT scanning the early days.* British Journal of Radiology, 2006. 79(937): p. 5-8.

2. Ter-Pogossian, M.M., et al., *A positron-emission transaxial tomograph for nuclear imaging (PETT).* Radiology, 1975. 114(1): p. 89-98.

3. Hendee, W.R., *Physics and applications of medical imaging.* Reviews of Modern Physics, 1999. 71(2): p. S444-S450.

4. Daly, S.M. and M.J. Leahy, *'Go with the flow ': a review of methods and advancements in blood flow imaging.* J Biophotonics, 2013. 6(3): p. 217-55.

5. Tung, C.H., et al., *In vivo imaging of proteolytic enzyme activity using a novel molecular reporter.* Cancer Research, 2000. 60(17): p. 4953-4958.

6. Ntziachristos, V., et al., *Looking and listening to light: the evolution of whole-body photonic imaging.* Nature Biotechnology, 2005. 23(3): p. 313-320.

7. Herschman, H.R., *Molecular imaging: Looking at problems, seeing solutions.* Science, 2003. 302(5645): p. 605-608.

8. Willmann, J.K., et al., *Molecular imaging in drug development.* Nature Reviews Drug Discovery, 2008. 7(7): p. 591-607.

9. Townsend, D.W. and S.R. Cherry, *Combining anatomy and function: the path to true image fusion.* European Radiology, 2001. 11(10): p. 1968-1974.

10. Hasegawa, B.H., et al., *Dual-modality Imaging of function and physiology.* Academic Radiology, 2002. 9(11): p. 1305-1321.

11. Cherry, S.R., *Multimodality in vivo imaging systems: Twice the power or double the trouble?* Annual Review of Biomedical Engineering, 2006. 8: p. 35-62.

12. Yang, H., et al., *Soft ultrasound priors in optoacoustic reconstruction: Improving clinical vascular imaging.* Photoacoustics, 2020. 19: p. 100172.

13. Ma, X., et al., *Integrin-Targeted Hybrid Fluorescence Molecular Tomography/X-ray Computed Tomography for Imaging Tumor Progression and Early Response in Non-Small Cell Lung Cancer.* Neoplasia, 2017. 19(1): p. 8-16.

14. Vitor, T., et al., *PET/MRI: a novel hybrid imaging technique. Major clinical indications and preliminary experience in Brazil.* Einstein (Sao Paulo, Brazil), 2017. 15(1): p. 115-118.

15. Pichler, B.J., et al., *Positron emission tomography/magnetic resonance imaging: the next generation of multimodality imaging?* Seminars in nuclear medicine, 2008. 38(3): p. 199-208.

16. Taruttis, A. and V. Ntziachristos, *Advances in real-time multispectral optoacoustic imaging and its applications.* Nature Photonics, 2015. 9(4): p. 219-227.

17. Wang, L.H.V. and S. Hu, *Photoacoustic Tomography: In Vivo Imaging from Organelles to Organs.* Science, 2012. 335(6075): p. 1458-1462.

18. Lutzweiler, C. and D. Razansky, *Optoacoustic Imaging and Tomography: Reconstruction Approaches and Outstanding Challenges in Image Performance and Quantification.* Sensors, 2013. 13(6): p. 7345-7384.

19. Cox, B.T., et al., *k-space propagation models for acoustically heterogeneous media: Application to biomedical photoacoustics.* Journal of the Acoustical Society of America, 2007. 121(6): p. 3453-3464.

20. Dean-Ben, X.L., V. Ntziachristos, and D. Razansky, *Acceleration of Optoacoustic Model-Based Reconstruction Using Angular Image Discretization.* Ieee Transactions on Medical Imaging, 2012. 31(5): p. 1154-1162.

21. Gateau, J., A. Chekkoury, and V. Ntziachristos, *Ultra-wideband three-dimensional optoacoustic tomography.* Optics Letters, 2013. 38(22): p. 4671-4674.

22. Taruttis, A., et al., *Multiscale Multispectral Optoacoustic Tomography by a Stationary Wavelet Transform Prior to Unmixing.* Ieee Transactions on Medical Imaging, 2014. 33(5): p. 1194-1202.

23. Kim, C., et al., *Performance benchmarks of an array-based hand-held photoacoustic probe adapted from a clinical ultrasound system for non-invasive sentinel lymph node imaging.* Philosophical Transactions of the Royal Society a-Mathematical Physical and Engineering Sciences, 2011. 369(1955): p. 4644-4650.

24. Laufer, J., et al., *In vivo preclinical photoacoustic imaging of tumor vasculature development and therapy.* Journal of Biomedical Optics, 2012. 17(5).

25. Zhang, C., et al., *Reflection-mode submicron-resolution in vivo photoacoustic microscopy.* Journal of Biomedical Optics, 2012. 17(2).

26. Razansky, D., et al., *Multispectral opto-acoustic tomography of deep-seated fluorescent proteins in vivo.* Nature Photonics, 2009. 3(7): p. 412-417.

27. Li, M.L., et al., *Simultaneous molecular and hypoxia imaging of brain tumors in vivo using spectroscopic photoacoustic tomography.* Proceedings of the Ieee, 2008. 96(3): p. 481-489.

28. Razansky, D., A. Buehler, and V. Ntziachristos, *Volumetric real-time multispectral optoacoustic tomography of biomarkers.* Nature Protocols, 2011. 6(8): p. 1121-1129.

29. Glatz, J., et al., *Blind source unmixing in multi-spectral optoacoustic tomography.* Optics Express, 2011. 19(4): p. 3175-3184.

30. Bianchini, P. and A. Diaspro, *Second Harmonic Generation Microscopy (SHG)*, in *Encyclopedia of Biophysics*, G.C.K. Roberts, Editor. 2013, Springer Berlin Heidelberg: Berlin, Heidelberg. p. 2280-2283.

31. Jechow, A., et al., *Enhanced two-photon excited fluorescence from imaging agents using true thermal light.* Nature Photonics, 2013. 7(12): p. 973-976.

32. Huff, T.B. and J.X. Cheng, *In vivo coherent anti-Stokes Raman scattering imaging of sciatic nerve tissue.* J Microsc, 2007. 225(Pt 2): p. 175-82.

33. Chen, W., et al., *Nonlinear ultrasonic imaging in pulse-echo mode using Westervelt equation: a preliminary research.* Computer Assisted Surgery, 2019. 24(sup2): p. 54-61.

34. Varray, F., et al. *Acoustic nonlinearity parameter of tissue on echo mode: review and evaluation of the different approaches for B/A imaging*. in *2009 IEEE International Ultrasonics Symposium*. 2009.

35. Pasovic, M., et al., *Broadband Reduction of the Second Harmonic Distortion During Nonlinear Ultrasound Wave Propagation.* Ultrasound in Medicine and Biology, 2010. 36(10): p. 1568-1580.

36. Pasovic, M., et al., *Second harmonic inversion for ultrasound contrast harmonic imaging.* Physics in Medicine and Biology, 2011. 56(11): p. 3163-3180.

37. Tieng, Q.M. and V. Vegh, *Magnetic resonance imaging in nonlinear fields with nonlinear reconstruction.* Concepts in Magnetic Resonance Part B: Magnetic Resonance Engineering, 2011. 39B(3): p. 128-140.

38. Allen et al, *Generating photoacoustic signals using high-peak power pulsed laser diodes.* Proc. SPIE 5696, 2005: p. 233-242.

39. Zharov, V.P., *Ultrasharp nonlinear photothermal and photoacoustic resonances and holes beyond the spectral limit.* Nature Photonics, 2011. 5(2): p. 110-116.

40. Sarimollaoglu, M., et al., *Nonlinear photoacoustic signal amplification from single targets in absorption background.* Photoacoustics, 2014. 2(1): p. 1-11.

41. Danielli, A., et al., *Picosecond absorption relaxation measured with nanosecond laser photoacoustics.* Applied Physics Letters, 2010. 97(16).

42. Danielli, A., et al., *Nonlinear photoacoustic spectroscopy of hemoglobin.* Applied Physics Letters, 2015. 106(20).

43. Nam, S.Y., et al., *Nonlinear photoacoustic signal increase from endocytosis of gold nanoparticles.* Optics Letters, 2012. 37(22): p. 4708-4710.

44. Lai, P.X., et al., *Photoacoustically guided wavefront shaping for enhanced optical focusing in scattering media.* Nature Photonics, 2015. 9(2): p. 126-132.

45. Petrova, E., et al., *Using optoacoustic imaging for measuring the temperature dependence of Gruneisen parameter in optically absorbing solutions.* Optics Express, 2013. 21(21): p. 25077-25090.

46. Simandoux, O., et al., *Influence of nanoscale temperature rises on photoacoustic generation: Discrimination between optical absorbers based on thermal nonlinearity at high frequency.* Photoacoustics, 2015. 3(1): p. 20-5.

47. Yelleswarapu, C.S. and S.R. Kothapalli, *Nonlinear photoacoustics for measuring the nonlinear optical absorption coefficient.* Opt Express, 2010. 18(9): p. 9020-5.

48. Nedosekin, D.A., et al., *Super-Resolution Nonlinear Photothermal Microscopy.* Small, 2014. 10(1): p. 135-142.

49. al, A.e., *Ultra-broadband photoacoustic imaging of label-free psoriasis biomarkers.* Nature Biomedical Engineering 1, 2017. 0068.

50. al, C.e., *All-optical photoacoustic microscopy.* PACS, 2015. 3(4): p. 143–150.

51. Di Ninni, P., F. Martelli, and G. Zaccanti, *Intralipid: towards a diffusive reference standard for optical tissue phantoms.* Physics in Medicine and Biology, 2011. 56(2): p. N21-N28.

52. Oraevsky, A.A., S.L. Jacques, and F.K. Tittel, *Measurement of tissue optical properties by time-resolved detection of laser-induced transient stress.* Applied Optics, 1997. 36(1): p. 402-415.

53. ANSI. 2000: The Laser Institute of America.

54. Chekkoury, A., et al., *Optical mesoscopy without the scatter: broadband multispectral optoacoustic mesoscopy.* Biomed Opt Express, 2015. 6(9): p. 3134-48.

55. Han, Y., et al., *Three-dimensional optoacoustic reconstruction using fast sparse representation.* Opt Lett, 2017. 42(5): p. 979-982.

56. Shaw, C.B., et al., *Least squares QR-based decomposition provides an efficient way of computing optimal regularization parameter in photoacoustic tomography.* J Biomed Opt, 2013. 18(8): p. 80501.

57. Calasso, I.G., W. Craig, and G.J. Diebold, *Photoacoustic Point Source.* Physical Review Letters, 2001. 86(16): p. 3550-3553.

58. Tian, C., et al., *Dual-pulse nonlinear photoacoustic technique: a practical investigation.* Biomedical optics express, 2015. 6(8): p. 2923-2933.

59. A. Dima; N. C. Burton and V. Ntziachristos, *Multispectral optoacoustic tomography at 64, 128, and 256 channels.* J Biomed Opt, 2014. 19: p. 36021.

60. Wang, W. and A. Mandelis, *Microwave-heating-coupled photoacoustic radar for tissue diagnostic imaging.* Journal of Biomedical Optics, 2016. 21(6).

61. Kell, G.S., *Precise representation of volume properties of water at one atmosphere.* Journal of Chemical & Engineering Data, 1967. 12(1): p. 66-69.

62. Prakash, J., et al., *Short-wavelength optoacoustic spectroscopy based on water muting.* Proceedings of the National Academy of Sciences, 2020. 117(8): p. 4007.

63. Langford, V.S., A.J. McKinley, and T.I. Quickenden, *Temperature Dependence of the Visible-Near-Infrared Absorption Spectrum of Liquid Water.* The Journal of Physical Chemistry A, 2001. 105(39): p. 8916-8921.

64. Kapil, J.C., S.K. Joshi, and A.K. Rai, *In situ photoacoustic investigations of some optically transparent samples like ice and snow.* Review of Scientific Instruments, 2003. 74(7): p. 3536-3543.

65. J. Malekzadeh-Najafabadi; J. Prakash; V. Ntziachristos, *Nonlinear optoacoustic readings from diffusive media at near infrared wavelengths.* J Biophotonics, e201600310, , 2017.

66. M. Pramanik and L. V. Wang, *Thermoacoustic and photoacoustic sensing of temperature.* J Biomed Opt. 14, 054024 2009.

67. Boyd, R.W., *Nonlinear Optics*. Third ed. 2008: Elsevier.

68. Hutchins, D. and A.C. Tam, *Pulsed photoacoustic materials characterization.* IEEE Trans Ultrason Ferroelectr Freq Control, 1986. 33(5): p. 429-49.

69. H. M. Lai and K. Young, *Theory of the pulsed optoacoustic technique.* J. Acoust. Soc. Am. 72, 2000, 1982.

70. I. Brevik, *Experiments in phenomenological electrodynamics and the electromagnetic energy-momentum tensor.* Phys. Rep. , 1979. 52: p. 133.

71. Lou, C.G. and D. Xing, *Photoacoustic measurement of liquid viscosity.* Applied Physics Letters, 2010. 96(21).

72. Cao, Y.N. and G.J. Diebold, *Effects of heat conduction and viscosity on photoacoustic waves from droplets.* Optical Engineering, 1997. 36(2): p. 417-422.

73. Dean-Ben, X.L., V. Ntziachristos, and D. Razansky, *Acceleration of optoacoustic model-based reconstruction using angular image discretization.* IEEE Trans Med Imaging, 2012. 31(5): p. 1154-62.

74. T. Jetzfellner; D. Razansky; A. Rosenthal; R. Schulz; K.-H. Englmeie; and V. Ntziachristos, *Performance of iterative optoacoustic tomography with experimental data.* Appl. Phys. Lett., 2009. 95(1): p. 013703

75. C. C. Paige and M. A. Saunders, *LSQR: An algorithm for sparse linear equations ans sparse least squares.* ACM Trans. Math. Software, 1982. 8: p. 43-71